



Contents lists available at ScienceDirect

# Computer Methods in Applied Mechanics and Engineering

journal homepage: [www.elsevier.com/locate/cma](http://www.elsevier.com/locate/cma)



## Topology optimization for hybrid additive-subtractive manufacturing incorporating dynamic process planning

Shuzhi Xu <sup>a</sup>, Jikai Liu <sup>b,\*</sup>, Kentaro Yaji <sup>a</sup>, Lin Lu <sup>c</sup>

<sup>a</sup> Department of Mechanical Engineering, Graduate School of Engineering, Osaka University, 2-1, Yamadaoka, Suita, Osaka 565-0871, Japan

<sup>b</sup> Key Laboratory of High Efficiency and Clean Mechanical Manufacture (Ministry of Education), School of Mechanical Engineering, Shandong University, Jinan, China

<sup>c</sup> School of Computer Science and Technology, Shandong University, Qingdao, China



### ARTICLE INFO

#### Keywords:

Topology optimization  
Fabrication fields optimization  
Hybrid manufacturing  
Additive manufacturing  
Subtractive manufacturing

### ABSTRACT

Hybrid additive–subtractive manufacturing (HASM) is a revolutionary technique that, the interplay between additive and subtractive processes within an integrated machine tool allows for the fabrication of traditionally challenging complex geometries with excellent quality. However, part design for hybrid manufacturing has mostly been done by experts with rare support from computational design algorithms. Hence, the primary contribution of this work is to propose a solution for HASM-oriented structural topology optimization that incorporates both dynamic process planning and accessibility constraints. This novel optimization algorithm is developed under a unified SIMP and magic needle framework. Two sets of design variables are proposed: one for the topological description while the other for identifying the printing stage-related subdivisions. Accordingly, a series of additive manufacturing (AM) and subtractive manufacturing (SM) dedicated geometric constraints are developed based on these design variables to enable the cutting tool and laser head accessibility. Supported by the sensitivities, the structural geometry and fabrication fields can be simultaneously optimized. The effectiveness of the algorithm is proved through several numerical and experimental case studies. All the factors of cutting tool directions, HASM stages, and specific tool shapes are thorough investigated.

### 1. Introduction

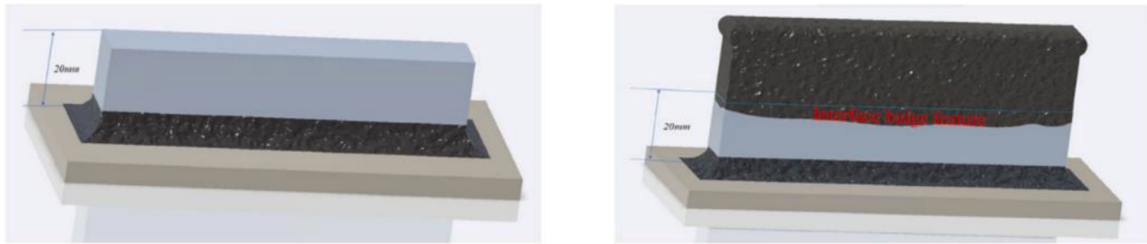
In recent years, the manufacturing industry has shown a growing interest in combining Additive Manufacturing (AM) and Subtractive Manufacturing (SM), capitalizing on 3D printing's ability to fabricate complex geometries with efficient material utilization and CNC machining's strength in achieving high geometric precision and delivering high-quality surface finishes. This type of hybrid manufacturing technology is commonly referred to as Hybrid Additive–Subtractive Manufacturing (HASM) [1–3]. Generally, AM is known for its layered material deposition that is capable of manufacturing complex structures, but the related shaping accuracy and surface quality cannot meet the requirements of precision engineering [4]. For amendment, HASM eliminates the shortcoming of AM by spontaneously finish machining the part [5,6]. Typical applications of HASM include the production of components for turbine blades with deep cavities, injection molds with conformal cooling channels, and engine heat exchangers incorporating regenerative cooling channels.

\* Corresponding author.

E-mail address: [jikai\\_liu@sdu.edu.cn](mailto:jikai_liu@sdu.edu.cn) (J. Liu).



**Fig. 1.** The DMG LASERTEC 65 3D Hybrid integrates an additive manufacturing system in the conventional CNC machine center.



(a) The first AM build plus SM finishing

(b) The second AM build and the formation of interface bulge feature due to remelting of and powder sputtering onto the already machined surface

**Fig. 2.** Formation of the interface bulge feature during interchanged AM-SM manufacturing [20].

With the advancement of manufacturing technology, topology optimization has emerged as a novel and increasingly prominent approach for design engineering [7–13]. In contrast to conventional structural (sizing and shape) optimization, topology optimization allows for the generation, merging, and splitting of interior voids [14–19], thus greatly expanding the design space, with the ability of achieving superior structural performance. Apart from the performance boost, topology optimization, tailored for HASM, can simultaneously satisfy the high demands on geometric precision, surface finishes, and cost-effectiveness, gradually becoming the latest research hotspot [20].

However, topology optimization features in deriving organic and complex structural geometry that can hardly be manufactured, even with the advanced HASM process [20]. The self-support issue and tool interference issue relieve but still exist for HASM. Furthermore, the thermo-mechanical manufacturing physics underlying the HASM process brings in difficulties in quality control [21]. Balancing the performance-driven freeform topological evolution and manufacturability-oriented material distribution restrictions has become a complex but unavoidable problem. There are typically two approaches to addressing this problem.

The first approach is to perform process planning for HASM that divides the part into subdivisions for the individualized additive-subtractive operations, thereby enabling the successful fabrication of a complex topological structure. Hybrid manufacturing is accomplished through a laser head that constructs 3D volumes by sintering materials layer by layer, and followed by a CNC machining cutter to remove materials and form the 3D sculptured surfaces [22]. A typical HASM platform (see Fig. 1) is equipped with 5-axis 3D printing and milling capabilities that alternatively take action [23]. The alternation of additive-subtractive operations divides the HASM process into a series of stages, here referred to as HASM stages. In each HASM stage, the laser head creates the 3D solid volume by laser sintering, and in the follow-up, a surface machining step processes the 3D surface of the solid volume with a fine finish (refer to Fig. 2) [20]. Process planning is the keystone to success a HASM task, since it creates the subdivisions and arranges the sequences of the

HASM stages [24]. Substantial progress has been made in addressing the process planning problem for HASM within the CAD/CAM community. However, the current status of hybrid manufacturing has not yet realized the extensive potential it holds. Many existing process planning practices still heavily depend on the expertise of operators [20].

There are a few studies that attempted to add search space restrictions to achieve process planning for HASM. These restrictions simplify the dynamic HASM accessibility and manufacturing dependency constraints, consequently reducing the problem-solving complexity [25–30]. A recent work [31] solves the general sequence planning problem without the above limitations. However, the pre-evaluation of mutual dependency between manufacturing sample points makes it unfriendly to the keep-evolving geometry in topology optimization.

Another approach is to enhance the structural design methodology to derive HASM-oriented structural solutions. This approach necessitates the simultaneous consideration of both AM and SM constraints at the structural design phase. Given AM processing, design for AM through topology optimization has gained significant attention over the past decade. Comprehensive reviews of the advancements and challenges in this area can be found in recent literature surveys [9–13]. In this context, length scale control is necessary for HASM-oriented topology optimization, because incorporating dimensional control constraints effectively prevents the generation of geometric features that are too fine to be printed by the AM laser spot or withstand the milling impact of the subtractive tool. The good aspect is that the controlling strategy and methods remain consistent with existing practices and requires no additional attention. The issue of calibrating printing paths demands careful attention since it can impact the shape-building quality, as well as the material property anisotropy [32–35]. Moreover, it is essential to give particular attention to the matter of process-induced residual stress and distortion. With laser or electron beam as the heat source, the rapid and repetitive heating and cooling cycles inevitably accumulate residual stresses inside the part body, leading to significant distortion of the part profile that can reach millimeter scale as reported in literature. Optimizing process parameters is an effective method to minimize part distortion [36–40]. Optimizing the structure redistributes residual stresses and thus functions to reduce residual distortion [41], as validated in numerous studies [42–48].

Design-for-SM is also critical since its extension is part of design-for-HASM. In its early stages, the concept of "design by feature" received the extensive attention, aiming to utilize 2.5D machining features to define parts [49–51]. Then, with the widespread adoption of 5-axis machining, the scenario of design-for-SM has evolved tremendously. In particular, these studies incorporate topology optimization-based freeform design methods, allowing unrestricted modifications to the geometry while simultaneously addressing the issue of cutting tool accessibility. However, topology optimization involves the free evolution of structures, often generating interior holes and undercuts that are inaccessible. Hence, the work in [52] have imposed constraints on the maximum curvatures of reentrant corners by controlling the minimum void length scale, ensuring tool accessibility. Subsequently, topology optimization advancement was developed to solve the 5-axis cutting tool accessibility issue. These approaches utilized a combination of density projections/machine learning with the SIMP method [53–58] and velocity field projection/distance function processing with the level set method [59,60].

HASM-oriented structural optimization research is still in its early stage, with only a few approaches developed to address the integration of AM and SM for manufacturing [61–63]. These previous works have not considered the interchange effect between AM and SM operations. The SM process in these studies is typically limited to 3-axis machining with pre-assigned feed directions. While for AM, it is limited to the self-supporting capability of the structure while does not address the rotating laser collision issue arising from process transformations. Furthermore, efforts have been made to utilize multi-axis SM as a post-processing method to address the support removal challenge associated with AM [64,65], but such methods only serve as a supplement to AM that cannot be categorized as a typical HASM scenario. Last but not least, there are significant simplifications in existing HASM-oriented topology optimization works. Specifically, these works typically predefine the domains for additive manufacturing and the regions for subtractive manufacturing, as well as their sequence. This type of simplification severely limits the degrees of design freedom that does not meet the actual scope of design for hybrid manufacturing. In summary, there is a clear gap in the development of topology optimization approaches dedicated to design-for-HASM. It is challenging to simultaneously address the accessibility issue associated to the rotating laser head and cutting tool, while consider the interchange effect between AM and SM operations. This type of algorithm is currently underdeveloped but has significant importance for designing novel functional structures to make full utilization of the characteristics of HASM.

The primary goal of HASM is to adopt the AM process to build the complex geometry and the SM process to ensure an excellent surface quality. In this work, we propose a novel topology optimization method for HASM, which incorporates dynamic process planning and full accessibility constraints on the interchanged AM and SM operations. HASM process planning for interchanged AM-SM operations are involved and simultaneously optimized with the overall topological structure. Dynamic process planning broadens the feasible design space of a manufacturable structure, especially compared with the conventional AM-first and SM-post processing scheme. Consequently, this approach allows for the augmentation in structural complexity, leading to a significant enhancement in the finally derived structural performance under the prerequisite of fully machining the part surface. Furthermore, compared to previous HASM-oriented design trials [61–63], this work considers the interchanged five-axis AM-SM operations that are counted as a true hybrid additive-subtractive manufacturing. It is highlighted that, two novel geometric constraints have been developed to tackle the interactions between AM and SM operations: the Additive Tool Collision Constraint and the Subtractive Tool Accessibility Constraint. They jointly impact the simultaneous optimization on the process plan and structural geometry. Additionally, the study also takes into consideration the structural self-supporting effect for eliminating supports.

The remaining content of this paper is structured as follows: [Section 2](#): introduction to the process plan optimization; [Section 3](#): detailed formulation of HASM-oriented geometric constraints, with [Section 3.1](#) covering the modeling of SM-oriented geometric constraints and [Section 3.2](#) describing the modeling of AM-related geometric constraints; [Section 4](#): introduction to the optimization problem formulation for HASM, as well as the numerical implementation details; [Section 5](#): presentation and discussion of several 2D

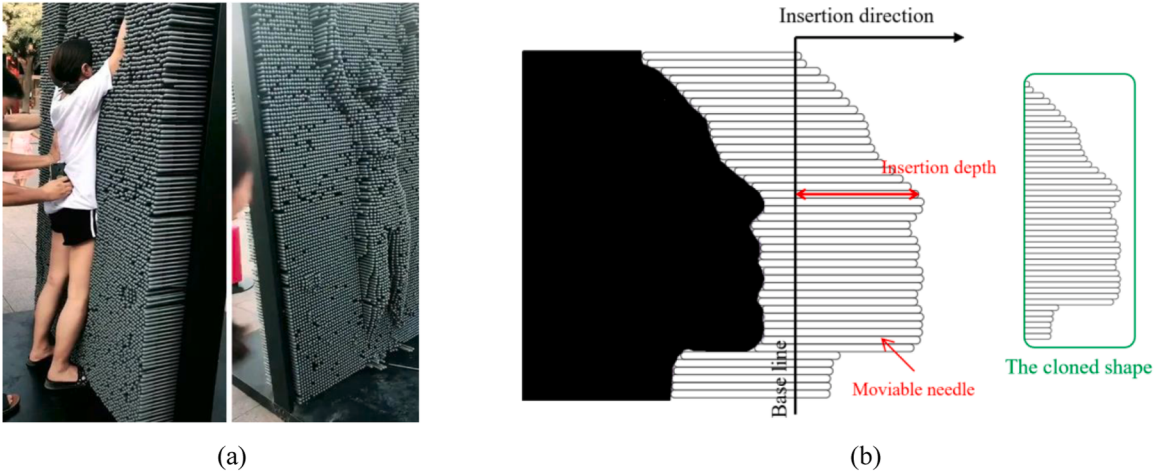


**Fig. 3.** (a) Illustration of the 3D magic needle cloning, (b) the schematic diagram of the magic needle cloning for 2D case.

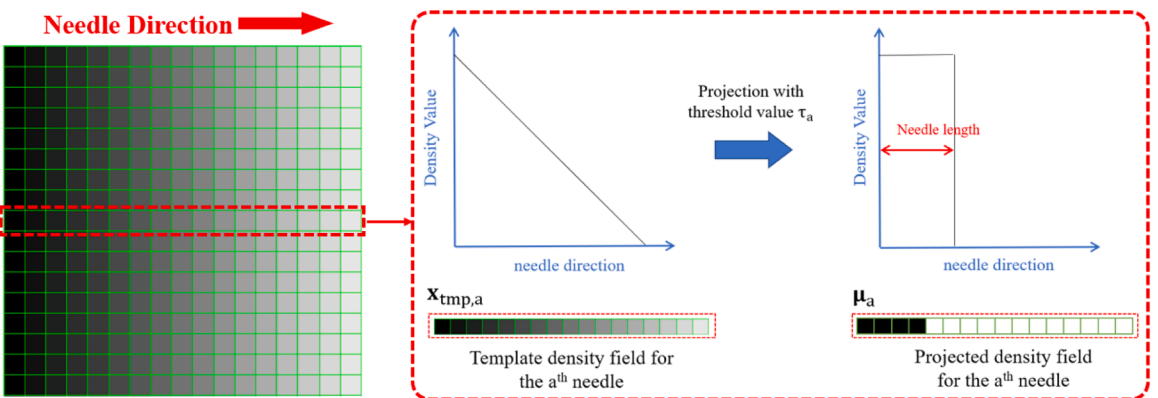


**Fig. 4.** Illustration of the control for the needle insertion.

and 3D benchmarks; **Section 6:** Experimental validation for the numerical results in 3D to prove the effectiveness of the proposed method; **Section 7:** conclusion that summarizes the key findings and contributions of the paper.

## 2. Process planning optimization for deriving subdivisions

The current paper focuses on HASM with alternating AM and SM operations in one integrated machine tool. For a structure with complexity, it will be fabricated through several HASM stages that each involves an AM and SM alternation. The density-based topology optimization framework is adopted to optimize the structure, and the magic needle method is adopted to create and optimize the subdivisions for deriving a feasible process plan. The design space  $\Omega$  is set as a square shape and discretized by a structured finite element mesh.

In incremental AM process, new materials are deposited onto the already built volume. In case of depositing without foundation, temporary auxiliary structures are utilized, known as support structure. For DED-type (Directed Energy Deposition) AM process, support structure is rarely used because of the high power input and non-trivialness in support removal. Hence, the material subdivisions provide foundations for the consequent material deposition following the fabrication sequence.

Recently, a novel form of artistic expression has emerged, known as 3D magic needle cloning, as depicted in Fig. 3(a). This technique uses a stationary frame that accommodates a number of patterned circular needles. Each circular needle can move along the longitudinal direction with two stopping positions. To further illustrate this mechanism, considering the 2D case in Fig. 3(b), when an object approaches the needles from one side, the needles are pushed forward so that on both sides, clone the corresponding shape of the object. If further enable elongation and shortening of the needles, the shapes cloned by the needles can be more flexible than those that do not have to be identical on the two sides. Hence, the set of needles can be regarded as the materials deposited in one hybrid manufacturing stage, and multiple sets of needles can be overlaid together to model the gap-free multi-stage hybrid manufacturing. The side shapes captured by the needles mimic the interfaces between different stages of additive depositions.

With the density-based optimization framework, the basic idea inspired by the magic needle mechanism is to represent densities in

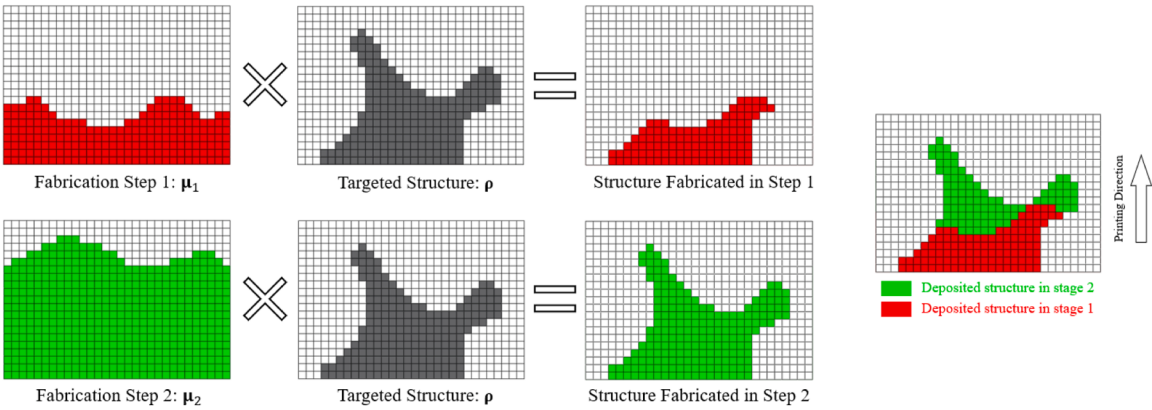


**Fig. 5.** Illustration of the subdivision identification for multi-stage manufacturing.

a row of elements using a single design variable to determinate the interface location between solid and void. As shown in Fig. 4, a density field is established at the left side as the template density field ( $x_{\text{Tmp}}$ ), and a uniform density gradient field is assumed along the needle direction. This template field contains multiple density strips that each strip represents one needle. Then, each density strip undergoes a Heaviside projection operation with a designated threshold. By adjusting these thresholds, denoted as strip-based thresholds ( $\tau$ ), precise control over the locations of the solid-void interface can be achieved [66]. A mapping relationship between the strip-based thresholds ( $\tau$ ) and element-wise thresholds ( $\alpha$ ) is introduced as:

$$\alpha = M\tau \quad (1)$$

where  $M$  is the binary mapping matrix with  $N_E \times N_d$  dimensions,  $N_E$  is the total number of finite elements in design space  $\Omega$ , and  $N_d$  is the total number of design variables (the number of strips). A relatively smaller density value indicates that this element is fabricated later. To ensure the smoothness of strip-based thresholds  $\tau$ , a smooth filter is applied:

$$\tilde{\tau} = T(\tau) \quad (2)$$

where the  $T(\cdot)$  is the smooth function. It could be any smooth filter commonly found in the field of topology optimization (like the PDE filter or convolution filter and so forth), for which the detail explanation could refer to [67]. The fabrication field by projecting the template densities could be expressed as [68]:

$$\mu = \frac{\tanh(\beta_F \tilde{M}\tilde{\tau}) + \tanh(\beta_F(x_{\text{Tmp}} - \tilde{M}\tilde{\tau}))}{\tanh(\beta_F \tilde{M}\tilde{\tau}) + \tanh(\beta_F(1 - \tilde{M}\tilde{\tau}))} \quad (3)$$

For multi-stage HASM process, we introduce multiple fabrication fields, and all the fabrication fields are projected based on the same  $x_{\text{Tmp}}$  but different thresholds:

$$\mu_n = \frac{\tanh(\beta_F \tilde{M}\tilde{\tau}_n) + \tanh(\beta_F(x_{\text{Tmp}} - \tilde{M}\tilde{\tau}_n))}{\tanh(\beta_F \tilde{M}\tilde{\tau}_n) + \tanh(\beta_F(1 - \tilde{M}\tilde{\tau}_n))}, \quad n = 1, 2, \dots, N_S \quad (4)$$

where  $N_S$  is the amount of fabrication stages.  $\mu_n$  indicates the area in  $\Omega$  that has been processed after the  $n^{\text{th}}$  HASM stage. To guarantee the material accumulation feature amongst the HASM stages, specific relationships are imposed to the strip-based thresholds ( $\tau_n$ ) and taking the  $a^{\text{th}}$  strip as example, the relationships are expressed as follows:

$$\begin{cases} \tau_{a,n} < \tau_{a,n-1}, \quad n \geq 2 \\ \tau_{\min} \leq \tau_{a,n} \leq 1 \end{cases} \quad (5)$$

By intersecting the density field  $\rho$  and each fabrication field  $\mu_n$ , the already-built structure after the  $n^{\text{th}}$  HASM stage could be explicitly modeled by:

$$\rho_n = \rho \circ \mu_n \quad (6)$$

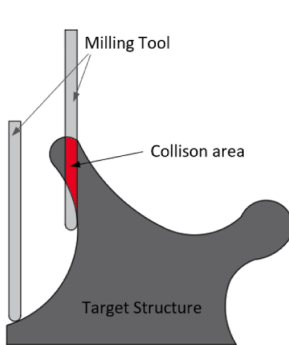
The symbol " $\circ$ " indicates the Hadamard product. Fig. 5 shows the identification of the stage-related subdivisions.  $\mu_1$  corresponds to the first stage AM-SM fabrication, and  $\mu_2$  represents the total volume after the second stage AM-SM fabrication. The density field ( $\rho$ ) means the physical structure. Through calculation with Eq. (6), the stage-based deposited subdivisions could be obtained, represented in red and green, respectively. Subsequently, the stage-based manufacturability constraints will be established based on these subdivisions.

At the end, we also want to provide a brief comparison between our proposed method and the existing space-time method [69]. Both methods share the common goal of optimizing fabrication regions within a density-based framework and employ the concept of

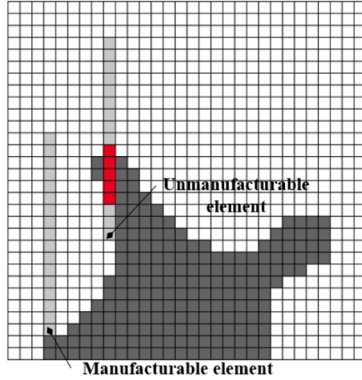
**Table 1**

Geometric constraints associated with HASM-oriented topology optimization.

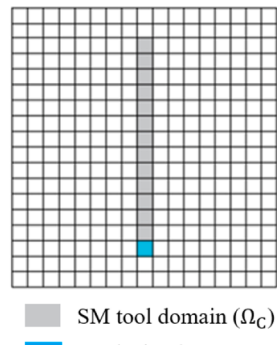
| HASM geometric constraints         |                                                                                                                                                        |                                           |                                                                                                                            |
|------------------------------------|--------------------------------------------------------------------------------------------------------------------------------------------------------|-------------------------------------------|----------------------------------------------------------------------------------------------------------------------------|
| AM (Additive manufacturing)        |                                                                                                                                                        | SM (Subtractive manufacturing)            |                                                                                                                            |
| Name                               | Description                                                                                                                                            | Name                                      | Description                                                                                                                |
| Length Scale Control               | Addressing the minimum printing resolution constraint on both solids and voids to guarantee the design printability.                                   | Subtractive Tool Accessibility Constraint | Ensuring collision-free access to the newly formed structural surface by the machining tool tip at every fabrication stage |
| Self-support Constraint            | Controlling the overhang inclination angles to eliminate the need of support structures, so that to improve the manufacturing and economic efficiency. |                                           |                                                                                                                            |
| Additive Tool Collision Constraint | Ensuring that in the current machining stage, the additive tool tip does not collide with the already built structure.                                 |                                           |                                                                                                                            |



(a)



(b)



(c)

**Fig. 6.** Illustration of the proposed accessibility analysis: (a) example of inaccessible condition; (b) the mesh for geometry in (a); (c) illustration of the SM tool domain  $\Omega_C$  and analysis element.

projection. However, there are key differences in their implementation. In the space-time method, the thresholds are fixed while the density magnitudes are optimized. This approach offers a larger space for optimization, but it may lead to numerical issues such as discontinuous processing regions and a higher likelihood of local optima. Although continuity constraints are employed to mitigate these issues, they are not always effective or stable. In contrast, our proposed method fixes the density magnitudes while optimizes the thresholds, focusing on mapping the continuous scale field through optimized thresholds. While this method imposes more limitations on the degrees of design freedom (but sufficiently large for 3-axis AM plus 5-axis SM), it ensures the regional continuity without any additional effort and involves fewer design variables.

### 3. Geometric constraints for hybrid additive-subtractive manufacturing

The HASM geometry constraints can be divided into two categories (as shown in [Table 1](#)): the AM oriented constraints and the SM oriented constraints. In [Section 3.1](#), the SM-oriented constraints are discussed, aiming at addressing the accessibility of multi-axis machining tool. Subsequently, in [Section 3.2](#), the focus shifts to the AM-related constraints, primarily considering length scale control (ensuring the resolution of the laser scanning qualified), structural self-support (no need for support structures in 3-axis AM), and no additive tool collision (ensuring the safety of the AM processing).

#### 3.1. Subtractive manufacturing constraint

In this Section, we will introduce the analytical accessibility analysis, wherein a continuous field is developed for quantifying the inaccessibility concerning a set of tools and fixtures. Subsequently, we perform the analysis of inaccessibility on the identified multiple subdivisions, and therefore, formulate the multi-stage inaccessibility constraint.

##### 3.1.1. Accessibility analysis

**3.1.1.1. Accessibility analysis for a single tool.** A part is manufacturable if all the void region within  $\Omega$  are accessible by the machining tool from the preassigned feeding direction, while making no intersection with the solid [53]. In order to meet the manufacturability

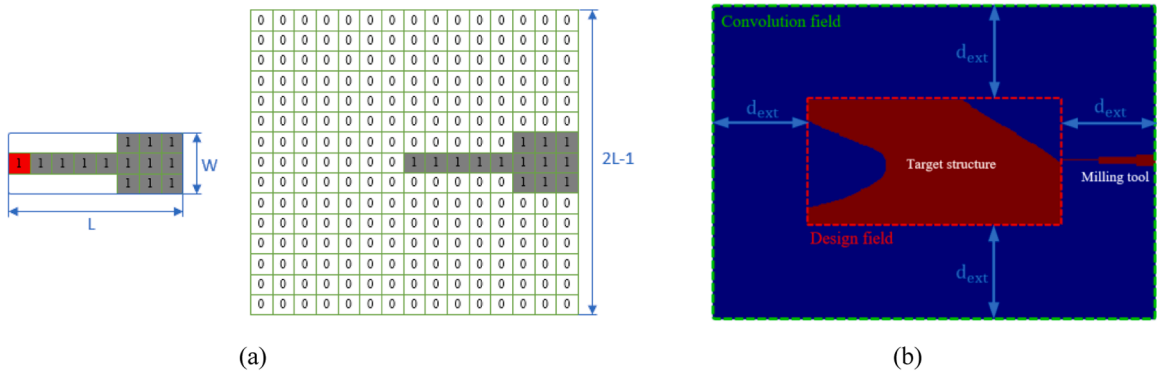


**Fig. 7.** Illustration of the SM tool and related convolution kernel (a); and the schematic diagram for the relationship between convolution field and design field (b).

requirement, this study proposes to construct a density field that increases monotonically in the milling direction based on Heaviside projection. The fundamental idea is to develop an analysis field:  $\psi$  that is separated from the physical field to indicate the manufacturability of the structure.

Given a specific element within the domain, its analysis density value is computed through averaging the cumulative sum of physical densities within the SM tool domain ( $\Omega_c$ ). Here,  $\Omega_c$  is established by tracking elements along the reverse milling direction as shown in Fig. 6(c), and its shape is constructed to mimic the shape of the tool. The above could be mathematically expressed as follows:

$$\tilde{\rho} = \frac{1}{N_c} \sum_{e \in \Omega_c} \rho_e \quad (7)$$

where  $N_c$  is the total number of elements in  $\Omega_c$ . The summed density of the analysis element serves as an indicator for manufacturability of the corresponding physical element at the same position. It has the following two situations:

- (1) The physical element density is 0 (void physical element): if its corresponding analysis element density has a value of zero, it means no physical block when the cutting tool approaches this element. Therefore, the physical element can be identified as manufacturable; if its corresponding analysis element density has a non-zero value, this physical element will be identified as unmanufacturable.
- (2) The physical element density is 1 (solid physical element): its corresponding analysis element density is consistently larger than zero, and there is no necessity to access this element for not involving material removal.

Here, more details are supplemented to the accessibility analysis for a concise implementation. First, a rectangular mesh consisting of squared finite elements is used to discretize both the physical and analysis fields. Second, given the invariant  $\Omega_c$ , Eq. (7) can be interpreted as a convolution operation.

For a 2-D situation, the convolution kernel  $\mathbf{x}$  is a 2-D binary square matrix, whose size is  $2\max(L, W) - 1$ , where  $L, W$ , are the length and width of  $\Omega_c$ , respectively; while for a 3-D situation, the convolution kernel  $\mathbf{x}$  is a 3-D binary matrix, whose size is  $2\max(L, H, W) - 1$ , where  $L, H, W$  are the length, height, and width of  $\Omega_c$ , respectively. Fig. 7 (a) shows a 2D format of  $\mathbf{x}$ , which indicates a 2D tool of size  $8 \times 3$  that is feeding horizontally towards left. The analysis element locates at the center of the kernel. Then, the element-based Eq. (7) could be further formulated into the following field-based expression:

$$\tilde{\rho} = \frac{\text{Conv}(\rho, \mathbf{x})}{N_c} \quad (8)$$

where  $\text{Conv}(\cdot)$  is the convolution operator. To ensure the consistency of field size, the domain extension approach (similar to the padding operation in Convolutional Neural Networks) is adopted here (shown in Fig. 7 (b)), where inside the red-color dashed frame is the design variable field and outside it is the extended domain. The design field plus the extension field make the convolution field. The distance  $d_{ext}$  should at least equal the length of the milling tool. The extension is performed by adding a padding of void elements to the design domain. Even though extended, the final design of interest is still defined by the physical densities inside the design domain.

The analysis densities obtained from Eq. (8) fall in the range of [0, 1]. Heaviside projection is then performed to process  $\tilde{\rho}$  into the 0–1 physical density, yielding  $\bar{\rho}$ . For this step, a Heaviside function [70] is used:

$$\bar{\rho} = 1 - e^{-\beta_p \tilde{\rho}} + \tilde{\rho} \cdot e^{-\beta_p} \quad (9)$$

where  $\beta_p$  controls the steepness of the Heaviside projection curve. We use  $\beta_p = 32$  for 2D and  $\beta_p = 64$  for 3D examples in this work (note that  $\beta_p$  is a fixed value, not updated with the optimization iteration).

Through Eqs. (8) and (9), for a given structure and tool processing conditions (such as tool shape and feeding direction, etc.), we

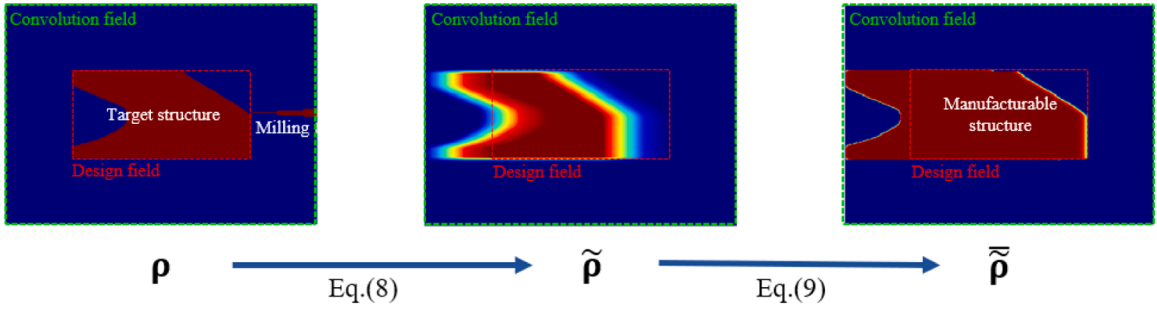


**Fig. 8.** Accessibility structure acquisition based on the accessibility analysis introduced in Section 3.1.1.

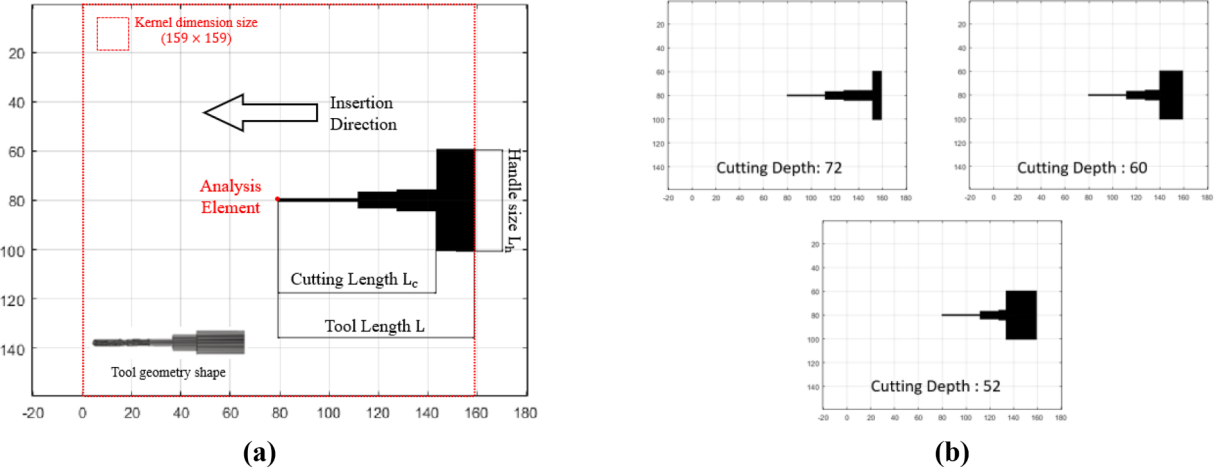


**Fig. 9.** The schematic diagram of the SM tool convolution kernel with specific tool geometry shape in 2D (a); and the SM tool convolution kernels with different cutting depths (b).

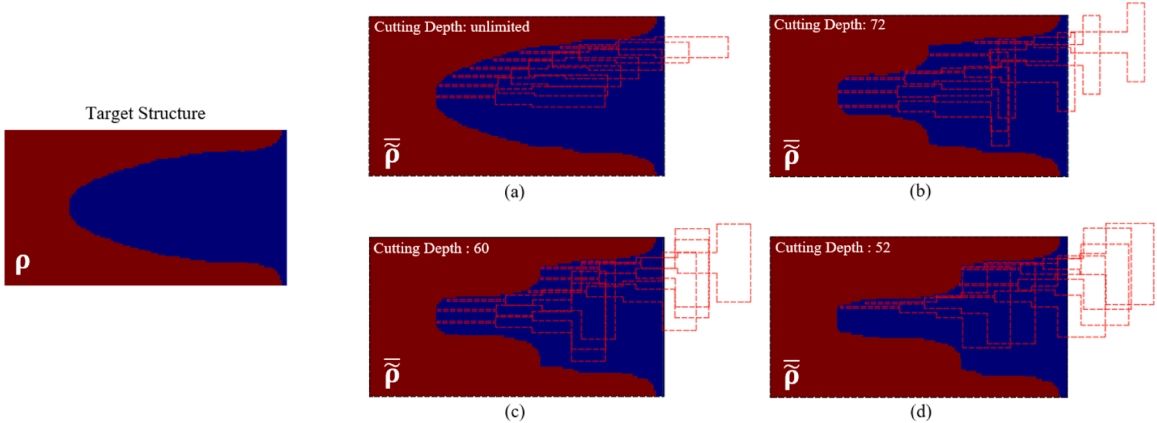


**Fig. 10.** The measured accessible fields with different cutting depths.

can get its corresponding machinable projection  $\bar{\rho}$ . Fig. 8 shows this process.

**3.1.1.2. Tool geometry control in accessibility analysis.** Obviously, the machinable structural shape is influenced by the tool geometry, e.g., the varying convolution kernel. Regardless of the tool geometry, the convolution kernel is configured only once, after which the information can be conveniently stored in  $\times$  for subsequent reuse during the optimization process. Hence, the investigation in this Section focuses on three aspects of the machining cutter: the configuration of tool geometry, the selection of feeding direction, and the

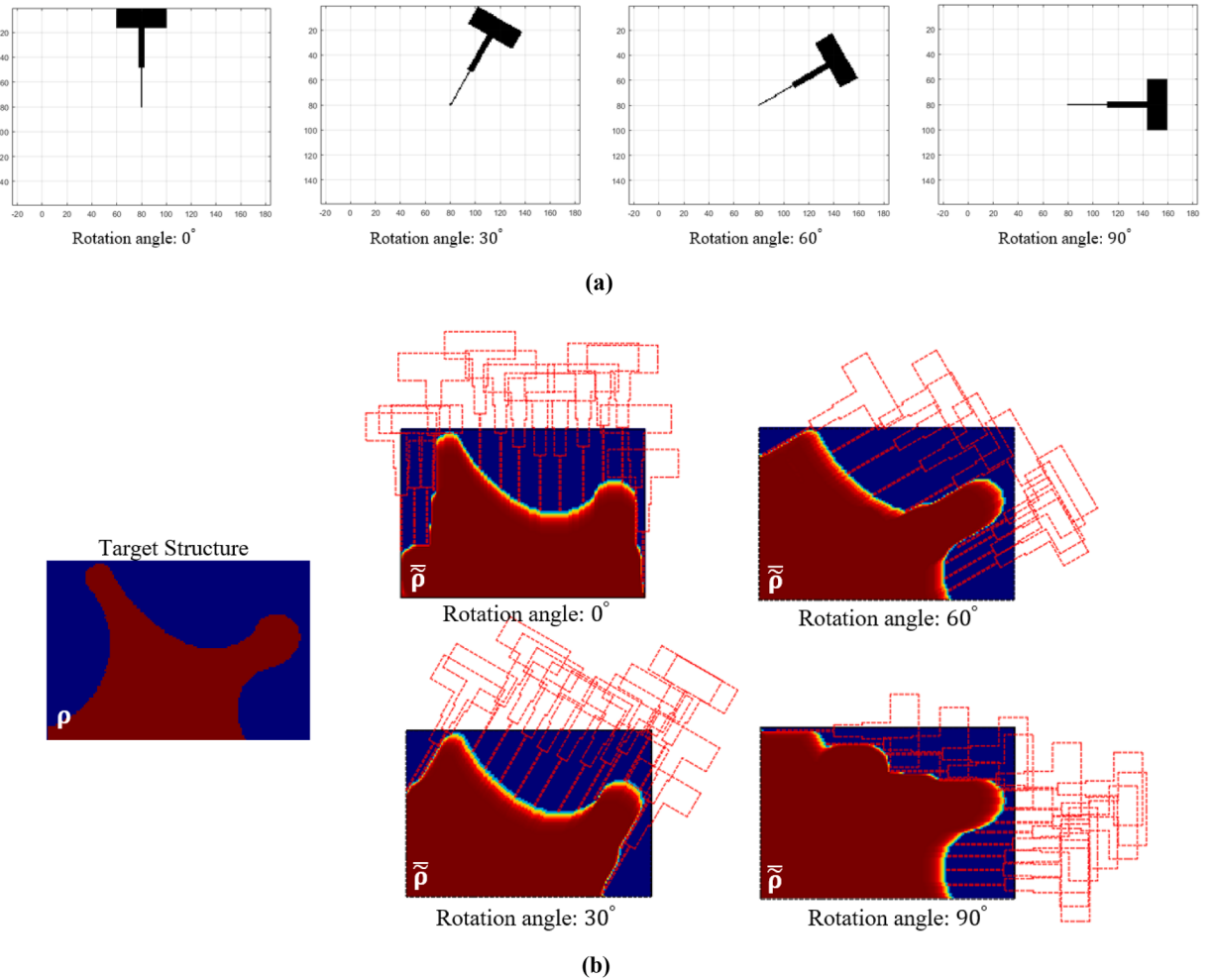


**Fig. 11.** The schematic diagram of kernel density field evolution for 2D rotations (a); and the measured accessible fields with different feeding directions (b).

determination of cutting depth.

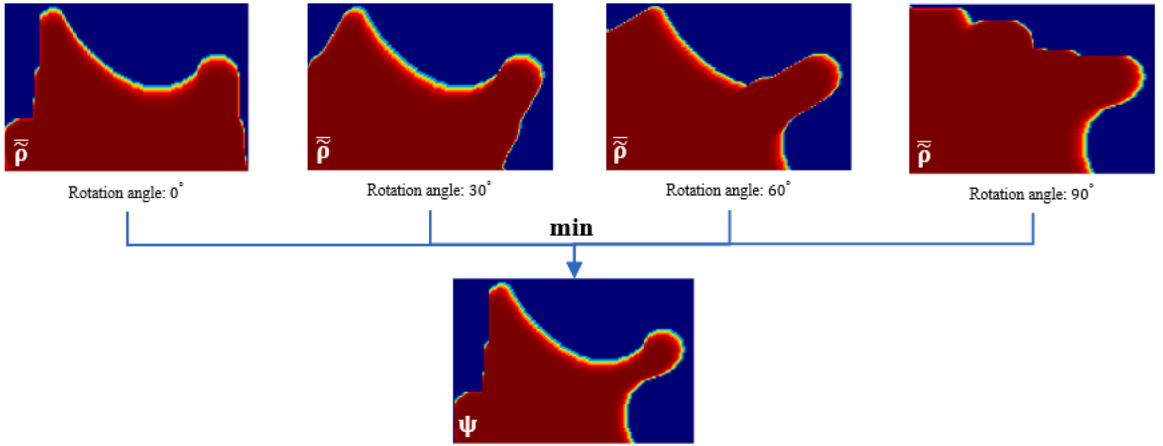
*The tool shapes.* To accommodate a specific tool shape, we adopt axisymmetric geometries as the primitive to build the tool. This axisymmetric entails representing tools using multiple diameters and segment lengths for the stepped rotation geometries.

Here, we illustrate the concept using an example 2-D milling tool. To facilitate the analysis, a handle is added to reflect the practical situation and then, the tool CAD model is discretized by  $80 \times 40$  elements, based on its actual dimensions. As a result, the corresponding tool kernel is a square matrix with the dimensions of  $159 \times 159$  (see Fig. 9 (a)).

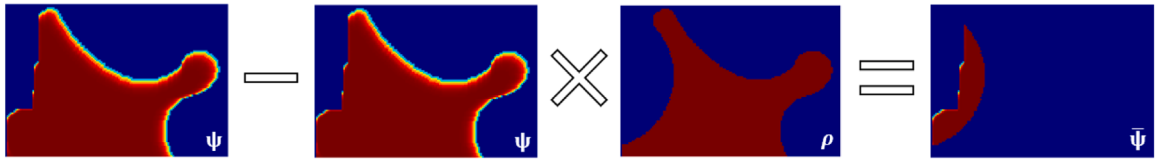
The next aspect to consider in milling tool geometry is about imposing the maximum cutting depth restriction, also known as the maximum insertion depth restriction, to avoid the tool holder or spindle to interfere with the part. One straightforward approach of imposing this restriction is to introduce a handle structure that has a significantly larger radius ( $L_h$ ) to mimic the tool holder. The distance ( $L_c$ ) between the left surface of the handle structure and the cutting tool tip, along the insertion direction, serves as the maximum cutting depth. In general, geometric features with a depth smaller than the cutting length  $L_c$  should remain unaffected by the cutting depth restriction. Fig. 9 (b) illustrates the cutting tool configurations with three different cutting depths, in which the thickness of the handle structure changes to keep a constant kernel size.

Fig. 10 illustrates the analysis results obtained from the similar tools with different cutting depths. When dealing with a target structure characterized by a deep hole feature, the cutting depth evidently influences the maximum machinable area. According to Fig. 10(a), when enabling an unlimited cutting depth, the deep hole feature is fully machined. However, when employing a restricted cutting depth, the deep hole feature can only be partially processed that is finished into a step hole (Fig. 10(b-d)). Hence, incorporating multi-stage hybrid manufacturing is necessary to fabricate deep hole structures if considering the limited cutting depth of a practical machining cutter.

*The feeding direction.* To conveniently implement the cumulative summation given an arbitrary direction, an affine transformation is applied to the kernel density field  $\rho$  defined in the reference local coordinate system, resulting in a mapped density field  $\rho_m$ :



**Fig. 12.** The schematic diagram for the aggregation of accessible structures from multiple feeding directions.



**Fig. 13.** The schematic diagram for the inaccessibility field identification.

$$\boldsymbol{x}_m = \mathbf{R}(\theta_m) \boldsymbol{x} \mathbf{R}(\theta_m)^T \quad (10)$$

in which  $\mathbf{R}(\theta_m)$  is the rotation matrix and  $\theta_m$  is the  $m^{\text{th}}$  feeding direction. The convolution kernel size remains unchanged regardless of the rotation angle, while the only change is the altered kernel density distribution. Fig. 11 (a) shows the 2D convolution kernel density fields for 4 different feeding orientations.

Then, using these rotated convolution kernels, each transformed convolution measures the accessible field for a target structure through the following equation:

$$\tilde{\rho}_m = \frac{\text{Conv}(\rho, \boldsymbol{x}, \theta_m)}{N_c} \quad (11)$$

Fig. 11 (b) illustrates the idea behind Eq. (11) for a simple 2D geometry with the four candidate orientations.

**3.1.1.3. Accessibility analysis for multiple tool configuration.** The analysis density fields obtained from multiple feeding orientations must be combined into a single field ( $\psi$ ) for an overall accessibility evaluation. Each density field contains void regions that can be processed from the specific feeding direction. By taking the Boolean intersection, all accessible regions are merged to form the final machinable workpiece:  $\psi = \bar{\rho}_1 \cap \bar{\rho}_2 \cap \dots \cap \bar{\rho}_m$ . To enable a differentiable intersection operation, a P-mean function is used:

$$\psi = \left( \frac{1}{N_m} \sum_{m=1}^{N_m} \bar{\rho}_m^P \right)^{\frac{1}{P}} \quad (\psi \in [0, 1]) \quad (12)$$

$\psi = 0$  means the accessible voids, and  $\psi = 1$  represents the projected machinable solid structure.  $N_m$  is the number of tool orientations, and  $P$  is the aggregation parameter ( $P = -12$  is adopted in this work).

Fig. 12 shows the aggregation of four accessible structures from four different feeding directions. The overall accessible field  $\psi$  is obtained by picking up the minimum over all directions.

In conclusion, the whole process of accessibility analysis could be expressed in the following function form:

$$\psi = \text{SM}(\rho, \boldsymbol{x}, \theta) \quad (13)$$

where  $\rho$  is the target structure,  $\boldsymbol{x}$  is the standard tool kernel (which includes the tool geometry and cutting length information), and  $\theta$  is the set of available feeding directions ( $\theta = \{\theta_1, \theta_2, \dots, \theta_m\}$ ). (Fig. 13)

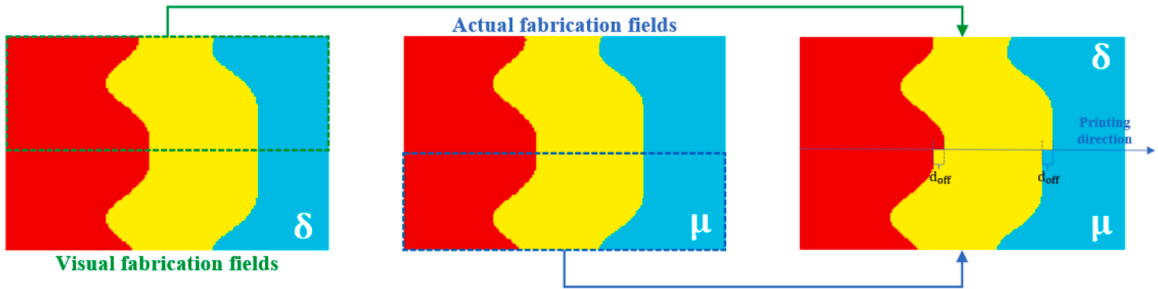


Fig. 14. The relationship between visual fabrication fields and actual fabrication fields.

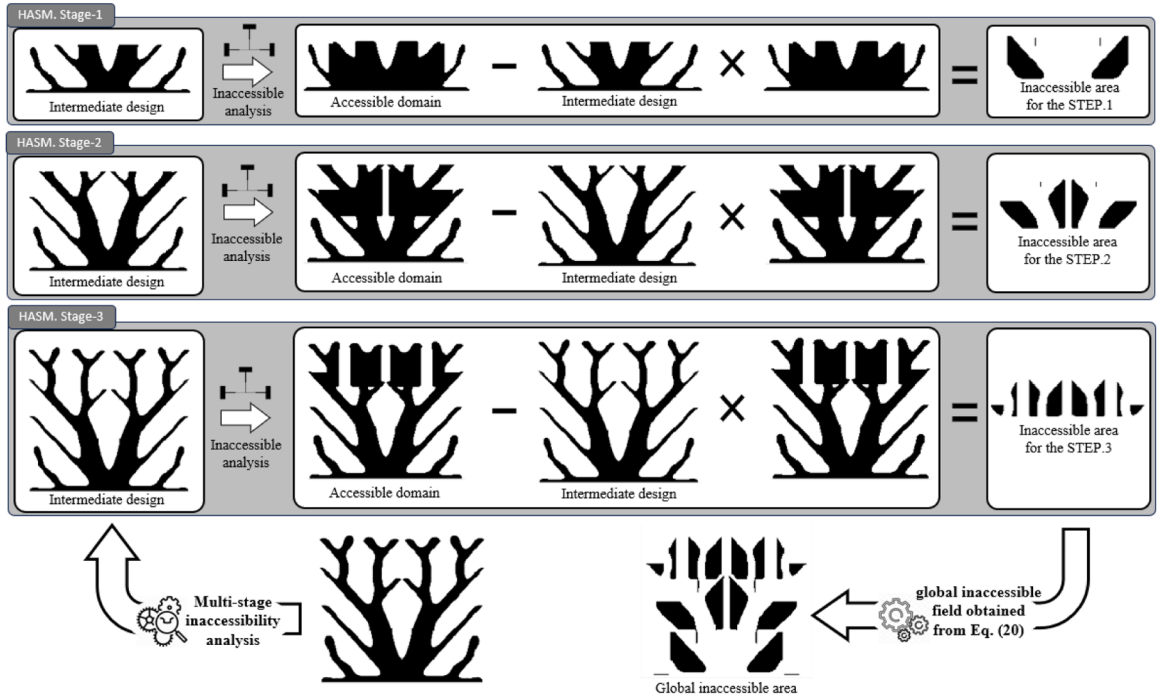


Fig. 15. The schematic diagram for subtractive inaccessible field identification of a three-stage hybrid manufacturing case.

### 3.1.2. Subtractive accessibility constraint

Based on the manufacturable structure  $\psi$  from Section 3.1.1, the corresponding inaccessible field ( $\bar{\psi}$ ) could be obtained through subtraction operation between the manufacturable structure and the target structure. This subtraction operation is formulated as:

$$\bar{\psi} = \psi - \psi \circ \rho \quad (14)$$

And the minimum inaccessible volume constraint is developed as:

$$\sum_{e=1}^{N_E} \bar{\psi}_e \leq V_{tol} \quad (15)$$

where  $N_E$  is the number of elements in the design domain  $\Omega$ , and  $V_{tol}$  represents the maximum-allowable inaccessible volume fraction.

This formulation of Eq. (14) is developed for several considerations. First, it avoids negative values, which can cause problematic evaluation on constraint Eq. (15). Second, it ensures that all density values in  $\bar{\psi}$  are confined within the range of 0 and 1. Third, it guarantees a smooth transition between inaccessible volumes and their adjacent volumes, avoiding sharp discontinuities. The above features enable a robust integration of the accessibility constraint with the employed topology optimization framework that stabilizes constraint solution process.

### 3.1.3. Multi-stage subtractive accessibility constraint

In each fabrication stage, the cutting tool will only process the structural surface of the newly deposited volume. Therefore, for the

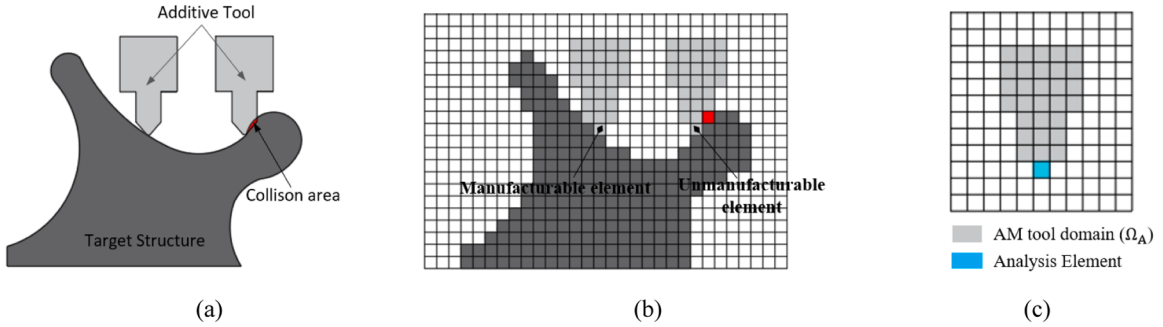


**Fig. 16.** (a) Example of AM tool collision; (b) the mesh for discretizing geometries in (a); (c) the illustration of additive tool domain  $\Omega_A$  and analysis element.

first fabrication stage, the accessible field of the incomplete structure is expressed by:

$$\psi_1 = \text{SM}(\rho_1, \alpha, \theta) \quad (16)$$

Starting from the second fabrication stage, the effective accessible field is calculated by:

$$\psi_n = \text{SM}(\rho_n, \alpha, \theta) \circ (\delta_n - \delta_{n-1}) \quad (17)$$

where  $\delta_n$  has the similar derivation with  $\mu_n$ , and its expression is:

$$\delta_n = \begin{cases} \frac{\tanh(\beta_F \mathbf{M}(\tilde{\tau}_n - \tau_{\text{off}})) + \tanh(\beta_F(\mathbf{x}_{\text{tmp}} - \mathbf{M}(\tilde{\tau}_n - \tau_{\text{off}})))}{\tanh(\beta_F \mathbf{M}(\tilde{\tau}_n - \tau_{\text{off}})) + \tanh(\beta_F(1 - \mathbf{M}(\tilde{\tau}_n - \tau_{\text{off}})))}, & n = 1, \dots, N_S - 1 \\ \mu_{N_S}, & n = N_S \end{cases} \quad (18)$$

In Eq. (17), the field  $(\delta_n - \delta_{n-1})$  indicates the  $n^{\text{th}}$  visual fabrication field, restricting the range of the inaccessible field judgement for the  $n^{\text{th}}$  stage fabrication. Note that, compared with the  $n^{\text{th}}$  actual fabrication field  $(\mu_n - \mu_{n-1})$ , the visual fabrication field is generated by upward offsetting a distance  $d_{\text{off}}$  along the build direction (Fig. 14), and the  $d_{\text{off}}$  is realized by tuning the parameter  $\tau_{\text{off}}$ . The purpose of this treatment is to prevent excessive material inaccessibility in the stage exchange area.

The corresponding  $n^{\text{th}}$  stage inaccessible field  $(\bar{\psi}_n)$  could be identified by:

$$\bar{\psi}_n = \psi_n - \psi_n \circ \rho_n \quad (19)$$

The global inaccessible field is then obtained by the following Boolean union operation:

$$\bar{\psi} = \sum_{n=1}^{N_S} \bar{\psi}_n \quad (20)$$

By restricting the global inaccessible field volume fraction to a minimum value  $V_{\text{tol}}$  (Eq. (15)), all surface elements of the design structure can be accessed by the multi-stage milling operation. Fig. 15 shows a detailed subtractive inaccessible area analysis on a 2D topology optimized heat conduction part subject to three HASM stages.

### 3.2. Additive manufacturing constraint

#### 3.2.1. Additive tool collision-free constraint

Similar to the subtractive accessibility analysis, an AM analysis field:  $\vartheta$ , is built on top of the physical field to measure the collision state of the current deposited structure, which uses the same reference mesh of the physical field.

Again, for a given element inside the design domain, its analysis density is computed by averaging the cumulative summation of the physical densities for all elements inside the additive tool domain ( $\Omega_A$ ), as shown in Fig. 16(c). The shape of  $\Omega_A$  is constructed by projecting the additive tool. The specific calculation could be expressed as follows:

$$\hat{\rho} = \frac{1}{N_A} \sum_{e \in \Omega_A} \rho_e \quad (0 < \hat{\rho} < 1) \quad (21)$$

where  $N_A$  is the total number of elements contained in  $\Omega_A$ . Similar to the subtractive accessibility analysis, the additive analysis density  $\hat{\rho}$  indicates the collision state of the corresponding physical element. If larger than 0, the tool collides with the already built part when the additive tool tip accesses this element. It is noted that, the collision analysis will start from the second HASM stage since the collision phenomenon will not appear during the initial-stage additive manufacturing. The convolution operation for Eq. (21) could be expressed as:

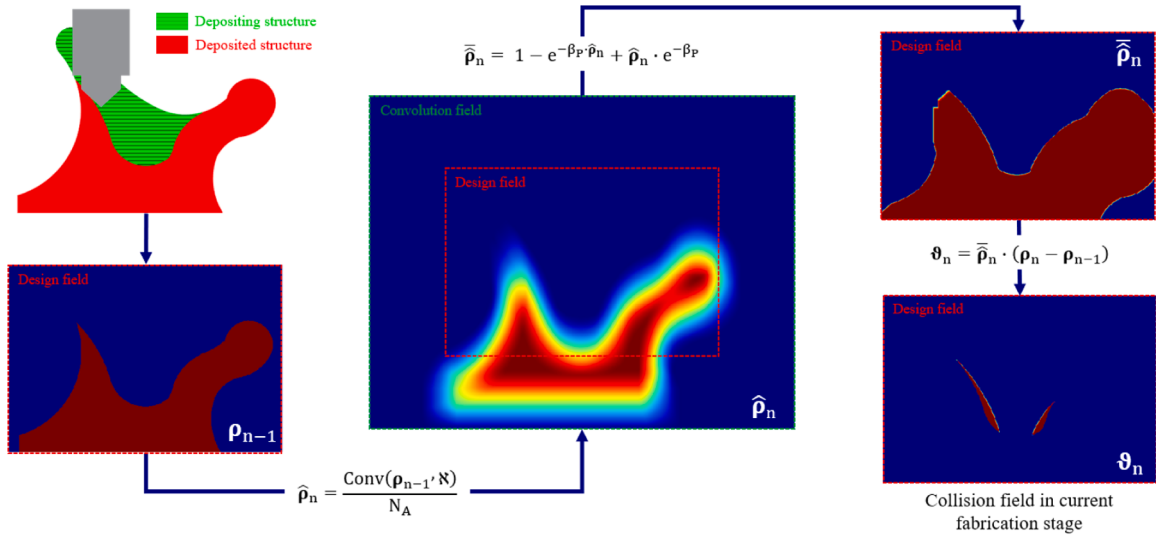


Fig. 17. The process for additive tool collision analysis.

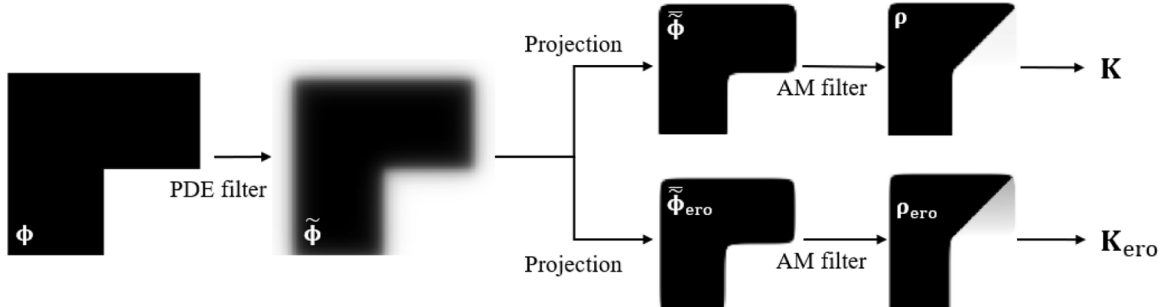


Fig. 18. The design parametrization for the targeted structure design.

$$\hat{\rho}_n = \frac{\text{Conv}(\rho_{n-1}, \aleph)}{N_A}, \quad n = 2, 3, \dots, N_s \quad (22)$$

where  $\rho_{n-1}$  is the structure built from the last stage, and  $\aleph$  is the AM tool convolution kernel. The Heaviside function is then used to map entries of  $\hat{\rho}_n$  into the 0 – 1 binary densities:

$$\bar{\rho}_n = 1 - e^{-\beta_p \cdot \hat{\rho}_n} + \hat{\rho}_n \cdot e^{-\beta_p} \quad (23)$$

In conclusion, the process of additive tool accessibility analysis could be summarized into the following function:

$$\bar{\rho}_n = \text{AM}(\rho_{n-1}, \aleph), \quad n = 2, 3, \dots, N_s \quad (24)$$

Given the fact that collisions only happen during depositing solid physical elements, the collision analysis for void physical elements can be disregarded. Consequently, the collision elements can be obtained by Boolean intersecting the current-stage depositing structure ( $\rho_n - \rho_{n-1}$ ) and collision-detected density field ( $\bar{\rho}_n$ ).

$$\theta_n = \bar{\rho}_n \cdot (\rho_n - \rho_{n-1}), \quad n = 2, 3, \dots, N_s \quad (25)$$

The global effective collision field is obtained through Boolean union operation:

$$\vartheta = \sum_{n=2}^{N_s} \theta_n \quad (26)$$

Finally, a non-collision constraint is developed to eliminate all element-wise collisions:

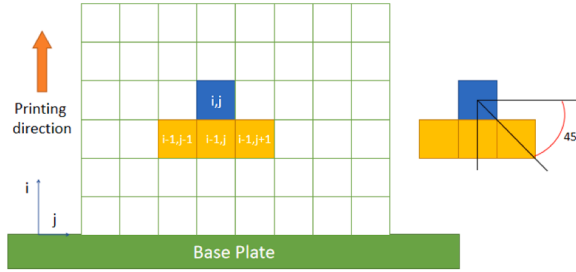


Fig. 19. The schematic diagram of the AM filter for 2D case.

$$\frac{1}{N_E} \sum_{e=1}^{N_E} \vartheta_e = V_{tol} \quad (27)$$

$V_{tol}$  used here represents the maximum-allowable collision volume fraction (generally, it has the same value with the  $V_{tol}$  shown in Eq. (15)). It is disclosed in Fig. 17 that, collisions occur when the inclination angle of the interface between two consecutive additive volumes becomes excessively large. Hence, the introduction of the constraint in Eq. (27) has a simultaneous effect on optimizing the interface flatness, tending to produce simple-shaped interfaces.

### 3.2.2. Minimum length scale control

For structures with too thin geometric features, it does not have enough strength to withstand the cutting force, leading to chatter or damage. To prevent structural failures, we adopt a simplified robust formulation to ensure the minimum length scale by considering both the erosion projection ( $\epsilon_{ero} > 0.5$ ) and intermediate projection ( $\epsilon = 0.5$ ). In the context of compliance minimization, the density field associated with the erosion projection is thinned and has a higher compliance compared with the intermediate density field. Therefore, including both the intermediate and erosion projections into the objective function indeed performs the minimum length scale control by warranting the thinned structure a sufficient stiffness. As shown in Fig. 18, other than projection for  $\bar{\phi}$ , the filtered field  $\tilde{\phi}$  is also projected to derive the so-called eroded field  $\bar{\phi}_{ero}$ :

$$\bar{\phi}_{ero} = \frac{\tanh(\beta_B \epsilon_{ero}) + \tanh(\beta_B (\tilde{\phi} - \epsilon_{ero}))}{\tanh(\beta_B \epsilon_{ero}) + \tanh(\beta_B (1 - \epsilon_{ero}))} \quad (28)$$

where  $\epsilon_{ero}$  is the erosion threshold. Then, both  $\bar{\phi}_{ero}$  and  $\tilde{\phi}$  will be further projected by the AM filter introduced in next section. Based on the Solid Isotropic Material with Penalization (SIMP) method, the elastic moduli of the  $e^{\text{th}}$  element for these two fields are interpolated as follows:

$$\begin{aligned} E_e(\bar{\phi}_e) &= E_{min} + (E_0 - E_{min}) \bar{\phi}_e^P \\ E_{ero,e}(\bar{\phi}_{ero,e}) &= E_{min} + (E_0 - E_{min}) \bar{\phi}_{ero,e}^P \end{aligned} \quad (29)$$

where  $E_0$  is the elastic modulus/conductivity of the solid material,  $E_{min}$  is a small value to avoid numerical singularity,  $P = 3$  is a penalty factor. Specifically, the simplified robust formulation is expressed as:

$$C_r = \omega U^T K U + (1 - \omega) U_{ero}^T K_{ero} U_{ero} \quad (30)$$

where  $\omega$  is a weighting factor, and the superscript  $ero$  in the second term indicates the erosion projected field.  $T$  is the transpose operator,  $U$  and  $U_{ero}$  are the response fields,  $K$  and  $K_{ero}$  are the stiffness matrices for the intermediate and erosion projected structures. The stiffness matrices  $K$  and  $K_{ero}$  are assembled from element stiffness matrices defined by  $k_e = E_e(\bar{\phi}_e) k_0$  and  $k_{ero,e} = E_{ero,e}(\bar{\phi}_{ero,e}) k_0$ , where  $k_0$  is the stiffness matrix of a solid element with unit Young's modulus/conductivity.

### 3.2.3. Formulation for the self-support AM filter

Then, to avoid the need for support structures, it is crucial to regulate the inclination angles of overhangs during the structural design. Hence, the utilization of self-support AM filter [71,72] is necessary.

Fig. 19 presents a 2D schematic diagram of the AM filter. The elements positioned on the lower layer are denoted by indices  $(i-1, j-1)$ ,  $(i, j-1)$ , and  $(i+1, j-1)$ , collectively referred to the support region for element  $(i, j)$ . When the support region lacks material, the AM filter removes materials from the corresponding element  $(i, j)$ . Conversely, if the support region contains material, the AM filter permits the presence of materials within element  $(i, j)$ . Consequently, these rules facilitate the attainment of self-supporting characteristics, featuring a  $45^\circ$  threshold overhang angle. Mathematically, the formulation of the AM filter is expressed as follows:

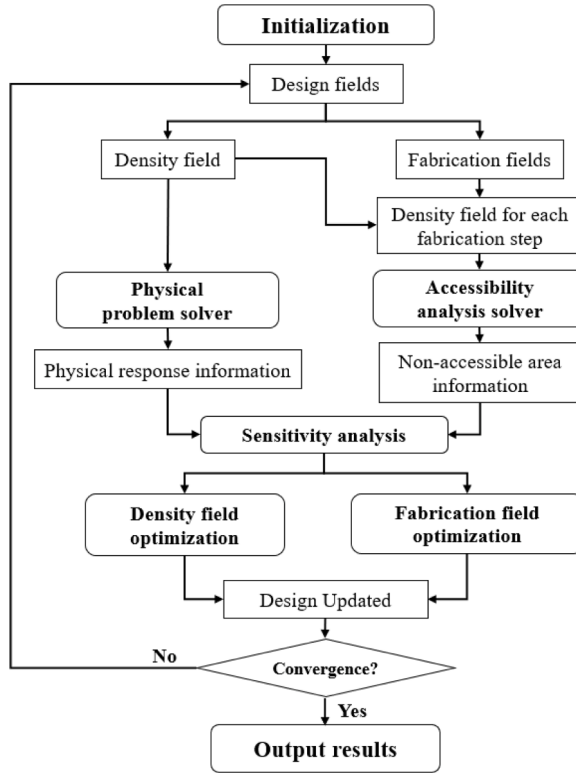


Fig. 20. The flowchart of the proposed method.

$$\rho_{ij} = \begin{cases} \min(\bar{\phi}_{ij}, \max(\bar{\phi}_{i-1,j-1}, \bar{\phi}_{ij-1}, \bar{\phi}_{i+1,j-1})) & (i,j) \in \Omega_u \\ \bar{\phi}_{ij} & (i,j) \in \Omega_b \end{cases} \quad (31)$$

Where  $\bar{\phi}$  is the density field obtained from the projection operation as mentioned in Section 3.2.1,  $\Omega_b$  means the field nearby the base plate, and  $\Omega_u$  means the rest of the design field above  $\Omega_b$ . The corresponding differentiable form is written as:

$$\rho_{ij} = \text{smin}(\bar{\phi}_{ij}, \text{smax}(\bar{\phi}_{i-1,j-1}, \bar{\phi}_{ij-1}, \bar{\phi}_{i+1,j-1})) \quad (i,j) \in \Omega_u \quad (32)$$

where smin is defined as:

$$\text{smin}(a, b) = \frac{1}{2} \left( a + b - \sqrt{(a - b)^2 + \epsilon_s^2} \right) \quad (i,j) \in \Omega_u \quad (33)$$

and smax is the P-Q max function used to calculate the maximum value of the elements in the supporting region:

$$\text{smax}(a, b, c) = \sqrt[Q]{(a^P + b^P + c^P)} \quad (i,j) \in \Omega_u \quad (34)$$

where  $\epsilon_s = 1e-4$  is the parameter that controls the accuracy of the approximation,  $P = 40$  and  $Q = P + \frac{\log(3)}{\log\left(\frac{1}{2}\right)}$  are used as suggested in [72].

#### 4. Numerical implementation

The proposed HASM-oriented topology-process simultaneous optimization is built on the compliance minimization problem. Two sets of optimization formulations are developed: the structural optimization and the process planning optimization, and these two optimization setups are tightly coupled together for an integrated implementation. For structural optimization, its formulation is stated as:

**Table 2**

The summary of the optimization schemes.

| Case name   | AM constraints | SM constraints | Multi-stage alternating tool | HASM stage optimization |
|-------------|----------------|----------------|------------------------------|-------------------------|
| AM-OPT      | ✓              | ✗              | ✗                            | ✗                       |
| HASM-OPT    | ✓              | ✓              | ✗                            | ✗                       |
| MulHASM-OPT | ✓              | ✓              | ✓                            | ✗                       |
| ProHASM-OPT | ✓              | ✓              | ✓                            | ✓                       |

$$\left\{ \begin{array}{l}
 \text{find : } \phi \\
 \text{minimize : } C_r(\phi) \\
 \\ 
 \text{subject to :} \left\{ \begin{array}{l}
 \mathbf{KU} = \mathbf{F} \quad (35-1) \\
 \mathbf{K}_{ero}\mathbf{U}_{ero} = \mathbf{F} \quad (35-2) \\
 \frac{\sum_{e=1}^{N_E} \rho_e}{N_E} \leq V_f \quad (35-3) \\
 \frac{\sum_{e=1}^{N_E} \bar{\psi}_e}{N_E} \leq V_{tol} \quad (35-4) \\
 \frac{\sum_{e=1}^{N_E} \vartheta_e}{N_E} \leq V_{tol} \quad (35-5) \\
 \phi_{\min} \leq \forall \phi_e \leq 1 \quad (35-6)
 \end{array} \right.
 \end{array} \right. \quad (35)$$

where  $\phi$  are the geometric design variables. Given process planning optimization, its formulation is stated as:

$$\left\{ \begin{array}{l}
 \text{find : } \tau_n \quad (n = 1, 2, \dots, N_s) \\
 \text{minimize : } g(\tau_n) \\
 \\ 
 \text{subject to :} \left\{ \begin{array}{l}
 \tau_{\min} \leq \forall \tau_{a,n} \leq 1 \quad (36-1) \\
 \tau_{a,n} < \tau_{a,n-1}, \quad n \geq 2 \quad (36-2)
 \end{array} \right.
 \end{array} \right. \quad (36)$$

where the design variables  $\tau_n$  ( $n = 1, 2, \dots, N_s$ ) determine the fabrication fields correlated to the HASM stages. The objective function  $g = \frac{\sum_{e=1}^{N_E} \bar{\psi}_e}{2N_E} + \frac{\sum_{e=1}^{N_E} \vartheta_e}{2N_E}$ , is developed by summing up the subtractive inaccessibility volume and additive tool collision volume.

The workflow of the proposed optimization process is given in Fig. 20. In this work, the HASM fabrication fields and the structure are simultaneously optimized. It can be seen from Fig. 20 that the accessibility analysis solver runs in every optimization loop to obtain the manufacturability information (subtractive tool accessibility and additive tool collision). A step-by-step description for the proposed implementation is outlined below:

1. Initialize the HASM fabrication fields and the topological density field. Initialize the accessibility analysis solver, physical problem solver, and optimization solver.
2. Run the physical problem solver and accessibility analysis solver to get the structural physical responses and the manufacturability information.
3. Calculate sensitivities on the topological density variables and HASM process planning variables based on the information from last step.
4. Updates the topological densities and HASM process planning variables.
5. Check for convergence criteria: if not satisfied, return to step 2; if satisfied, the results will be post-processed for visualization and manufacturing.

## 5. Numerical examples

In this numerical example section, the proposed method is applied to solve a heat conduction problem. This specific choice is made because the resulting part geometry tends to be complex, allowing for a sufficient validation of our method. In the 2D case, the discretization is made with 4-node first-order rectangle elements, while in the 3D case, 8-node first-order cube elements are utilized. The

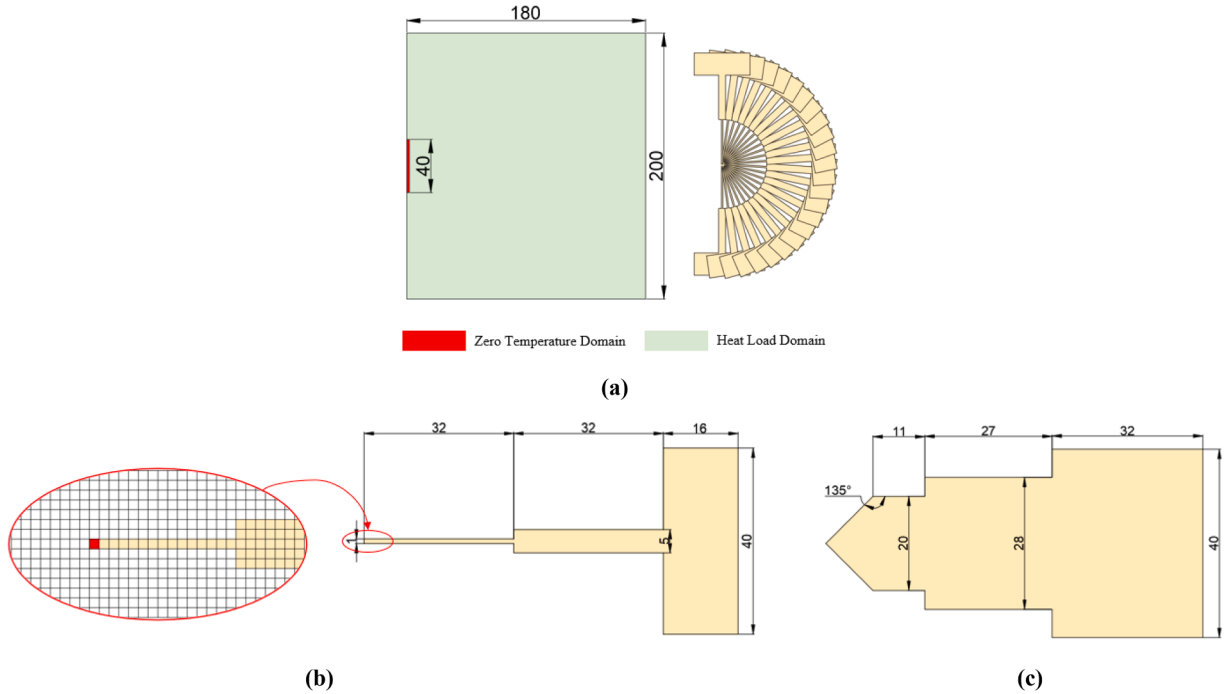


**Fig. 21.** The boundary condition and tool direction information for 2D heat conduction example (a); and the geometries of the SM tool (b) and AM tool (c).

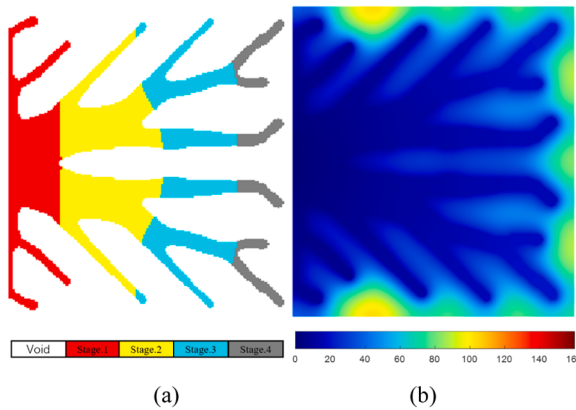


**Fig. 22.** The optimized design obtained from ProHASM-OPT (a) and its temperature distribution map (b).

smoothing filter employs the radius four times of the finite element size. The material layout design is updated using the Method of Moving Asymptotes (MMA) with a move limit of 0.2. The optimization process terminates when the objective function changes by less than 0.1 % over 5 successive iterations while all constraints are satisfied, or after a maximum of 250 iterations.

Four optimization cases are considered in this section: AM-OPT, HASM-OPT, MulHASM-OPT, and ProHASM-OPT. The various optimization schemes are detailed in Table 2.

### 5.1. 2-D example

The first numerical example is to design the heat conduction part in 2D, whose domain sizes are defined with  $L = 180\text{mm}$  and  $H = 200\text{mm}$ . The AM printing direction is left-right and the SM operation has 24 milling directions; see Fig. 21. A mesh with  $200 \times 180$  square elements of size  $1\text{mm} \times 1\text{mm}$  is employed to discretize the design space. The heat conductivity factor for the solid material is  $1 \text{W}/(\text{m} \cdot \text{K})$ , and a uniform heat load with  $10 \text{W}/\text{m}^2$  is applied in the design domain.

The boundary condition for this example is shown in Fig. 21 (a). In this example, the ProHASM-OPT optimization scheme involves 4 HASM stages. The mass fraction constraint for the designed structure is set to 30%. The shape information of the SM tool and AM tool

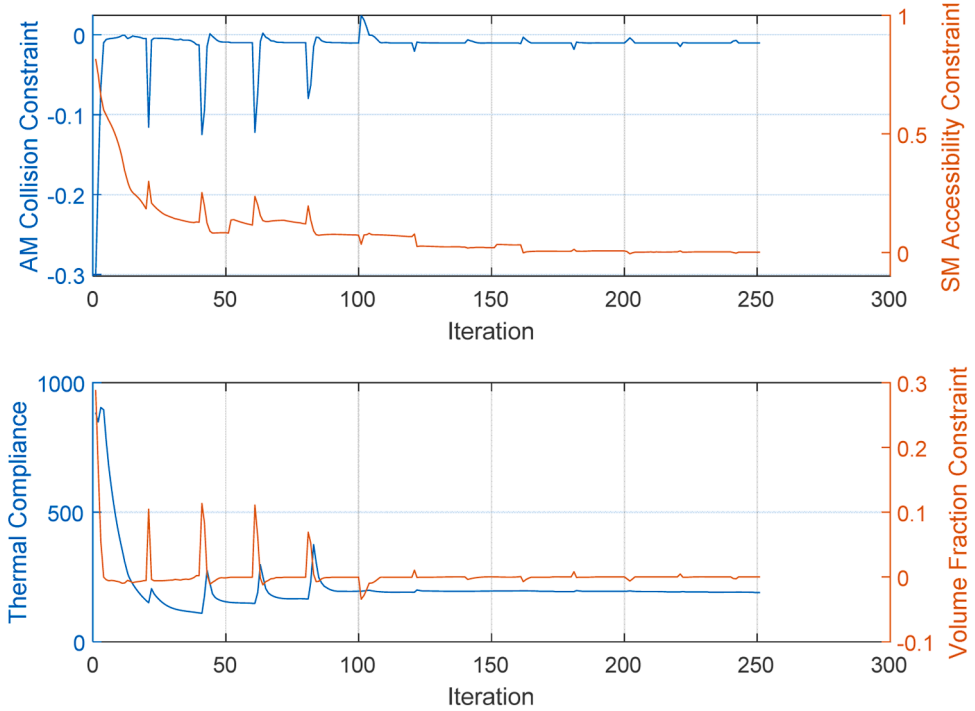


Fig. 23. The historical data of convergence information for ProHASM-OPT.

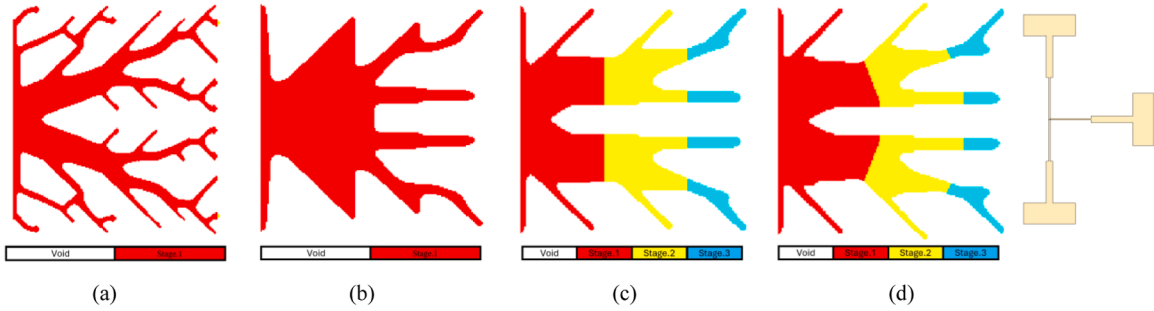


Fig. 24. The optimized designs obtained from AM-OPT (a), HASM-OPT (b), MulHASM-OPT (c), and ProHASM-OPT (d).

are provided in Fig. 21 (b) and (c).

Fig. 22 (a) displays the topologically optimized structure, and the associated temperature distribution is shown in Fig. 22 (b). The final thermal compliance is 206.7832J, and the maximum temperature is 75.69 K.

The historical data of convergence information is provided in Fig. 23. Due to the failure to meet the convergence criteria throughout, the optimization program was terminated after 250 iterations. However, the objective function value has almost stabilized during the final iterations. The multi-stage SM accessibility constraint, AM collision constraint, and volume fraction constraint have all been satisfied. By further examining the convergence history, during the first half of the optimization iterations, all curves exhibit significant oscillations, attributed to periodically updating the several Heaviside projection parameters. The oscillations eliminate during the second half of iterations owing to reaching a stable structural form. Hence, we can claim that this algorithm converges with a stable manner.

### 5.1.1. The comparison amongst different optimization schemes

Firstly, the influence of allowable SM tool orientations is investigated. To better distinguish the effects of different methods in this case, we constrain the direction of the subtractive tool to be perpendicular to the printing direction, along both inward and outward horizontal directions, totaling three directions.

Fig. 24 displays the optimized structures found from the four optimization schemes mentioned in Table 2. In the case of AM-OPT, the geometric complexity is the highest among the four schemes since it only considers the structural self-supporting constraint. However, as a consequence, many local geometric features cannot be processed by the cutting tool. HASM-OPT considers both the self-

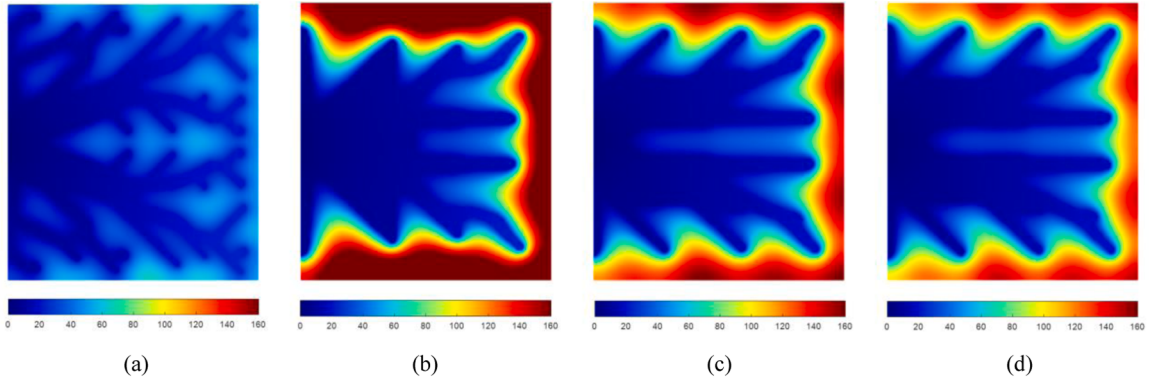


**Fig. 25.** The temperature distribution maps for the optimized designs obtained from AM-OPT (a), HASM-OPT (b), MulHASM-OPT (c), and ProHASM-OPT (d).

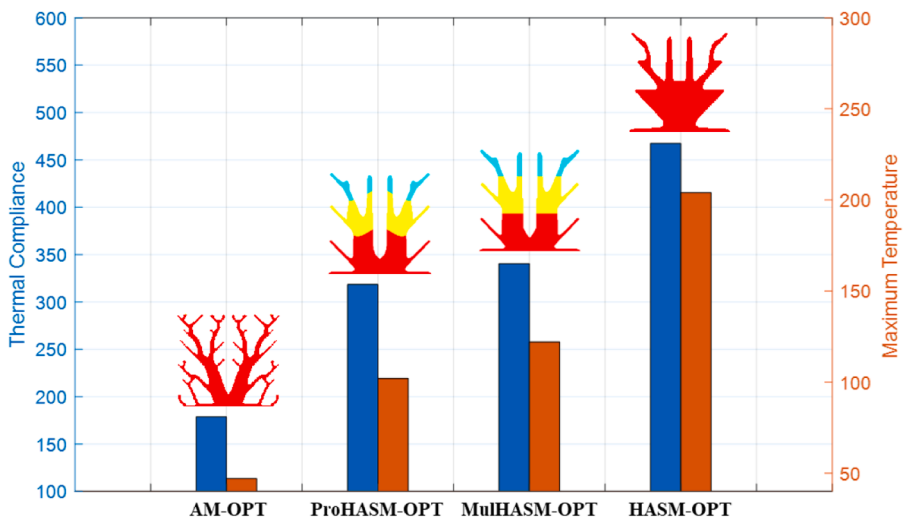


**Fig. 26.** The column chart for structural performance.

supporting constraint and the accessibility constraint of the cutting tool. As a result, its geometric complexity is strictly restricted, and all geometric features can be accessed by the cutting tool. Given MulHASM-OPT and ProHASM-OPT, compared with HASM-OPT, more geometric details emerge since they consider multiple AM-SM tool alterations. The resulted geometries from MulHASM-OPT and ProHASM-OPT are similar, but distinctions can be identified in local geometric details and also the inter-stage interfaces.

The temperature distribution maps for the four optimization schemes are displayed in Fig. 25. The maximum temperatures and the thermal compliances are summarized in Fig. 26. According to Fig. 26, the structural performance of AM-OPT (173.225J) is the best, followed by ProHASM-OPT (318.440J) and MulHASM-OPT (338.439J), while HASM-OPT (465.428J) performs the worst. Compared to MulHASM-OPT, the performance of ProHASM-OPT exhibits a slight improvement of approximately 5.4 %.

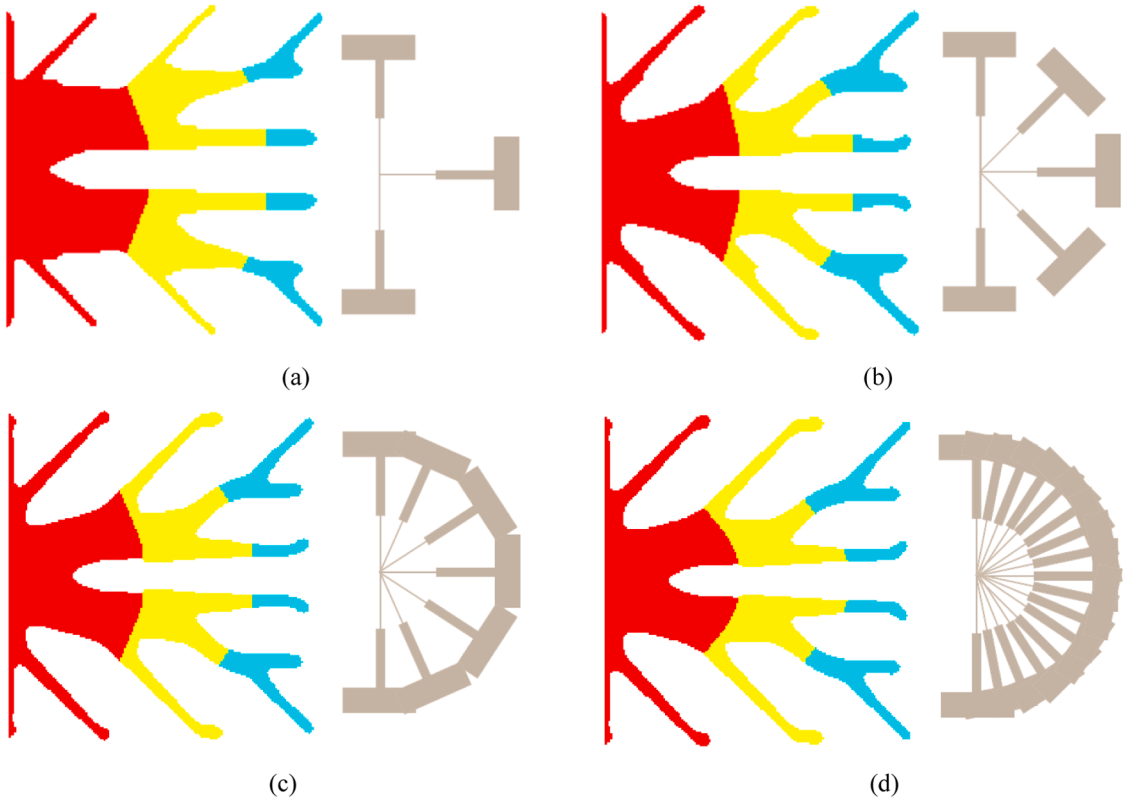
Hence, we can make preliminary conclusions from the above findings. Incorporating the SM tool accessibility constraint in structural optimization significantly restricts the available design space, consequently compromising structural performance. Then, accounting for the multi-stage HASM accessibility relieves the issue, reaching a better balance between structural performance and manufacturability, especially when the subdivisions are concurrently optimized.

### 5.1.2. The effect of allowable subtractive tool directions

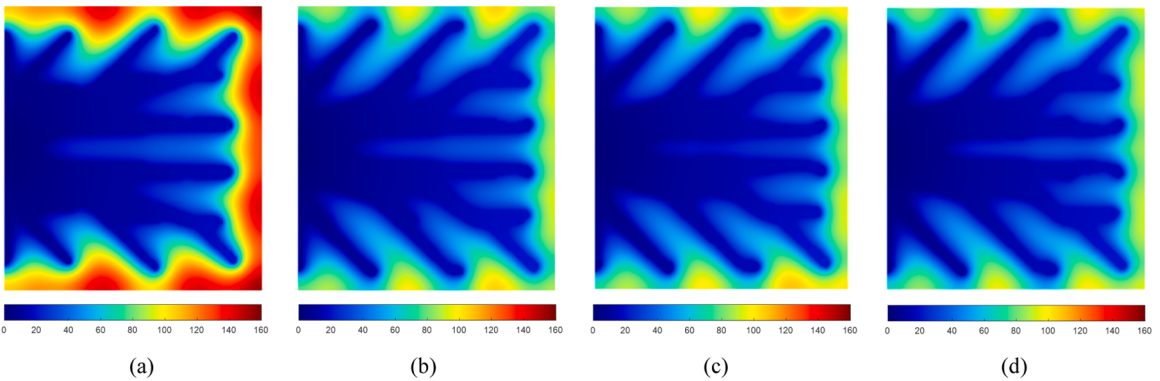
Subsequently the influence of allowable SM tool orientations is investigated. Four different combinations of SM tooling are considered, with 3, 5, 7, and 17 allowable directions, respectively. The shapes and dimensions of the SM and AM tools remain the same as Fig. 21. All other parameters remain consistent with Section 5.1.1.

Fig. 27 shows the optimized structures resulted from the four combinations of SM tools. Their final optimized thermal compliances are 318.440J, 265.113J, 251.567J, and 238.172J, respectively. It is evident that, more SM tool directions increase the geometrical complexity of the obtained structure.

The temperature distribution maps from the four SM tool combinations are displayed in Fig. 28. Compared with the ProHASM-OPT



**Fig. 27.** The optimized designs obtained from ProHASM-OPT with 3 tool orientations (a), 5 tool orientations (b), 7 tool orientations (c), and 17 tool orientations (d).



**Fig. 28.** The temperature distribution maps for the optimized designs obtained from ProHASM-OPT with 3 tool orientations (a), 5 tool orientations (b), 7 tool orientations (c), and 17 tool orientations (d).

with 3 SM tool orientations, the ProHASM-OPT with 17 SM tool orientations could achieve a 29 % performance improvement, and a 32 % reduction of the maximum temperature. For this considered problem, however, the performance improvement was limited when the set of tool orientations expanded beyond 5.

### 5.1.3. The effect of different HASM stages

In this Section, the effect of different amount of HASM stages will be investigated. Four scenarios are considered that involve 1 HASM stage, 2 HASM stages, 3 HASM stages, and 4 HASM stages, respectively. The tool dimensions and optimization parameters remain consistent with those described in Section 5.1.1. These numerical trials incorporate seven orientations for the subtractive tool.

Figs. 29,30 presents the optimized structures and its corresponding temperature distribution derived from the four trials. Their final thermal compliances are 366.163J, 298.127J, 251.567J, and 237.415J, respectively. It is evident that the more amount of HASM

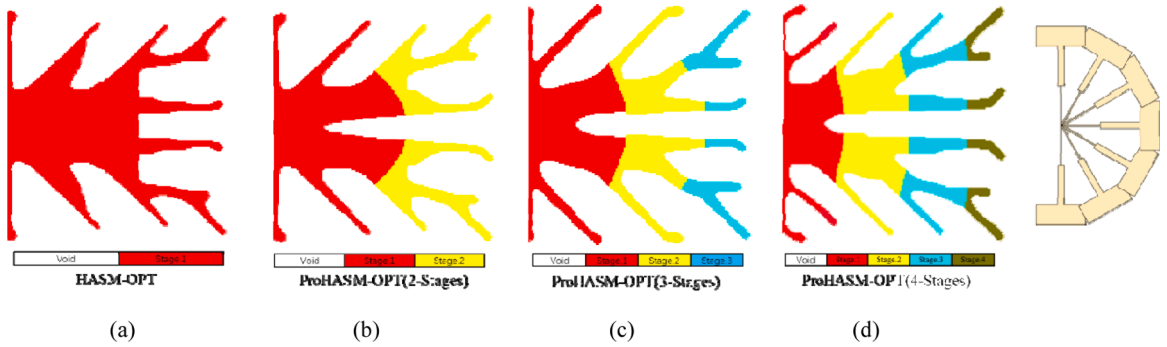


**Fig. 29.** The optimized designs obtained from HASM-OPT (a), and ProHASM-OPT with 2 HASM stages (b), 3 HASM stages (c), 4 HASM stages (d).

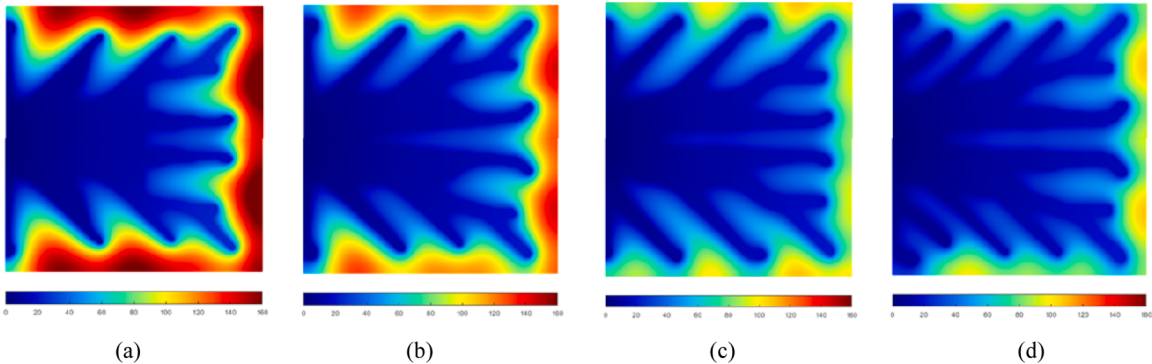


**Fig. 30.** The temperature distribution maps for the optimized design obtained from HASM-OPT (a), and ProHASM-OPT with 2 HASM stages (b), 3 HASM stages (c), 4 HASM stages (d).

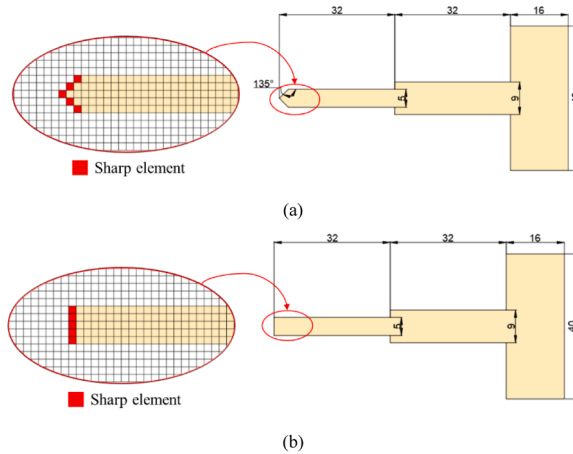


**Fig. 31.** The geometry information for the conic-tip SM tool (a) and the flat-tip SM tool (b).

stages leads to the increasing complexity of the structure. Some geometric features, such as deep holes which does not show in the HASM-OPT design, can be realized by the ProHASM-OPT configurations.

#### 5.1.4. The effect of different subtractive tool shapes

In this case, the cutting tools with flat and conic tips are considered as shown in Fig. 31 (a) and (b) to investigate the effect of varying SM tools on design. For these numerical trials, ProHASM-OPT with three HASM stages and three milling orientations are performed. The other optimization setups remain the same as the former cases.

Observing the designs presented in Fig. 32, it is evident that when compared to the default SM tool in Fig. 24 (d), the overall shapes

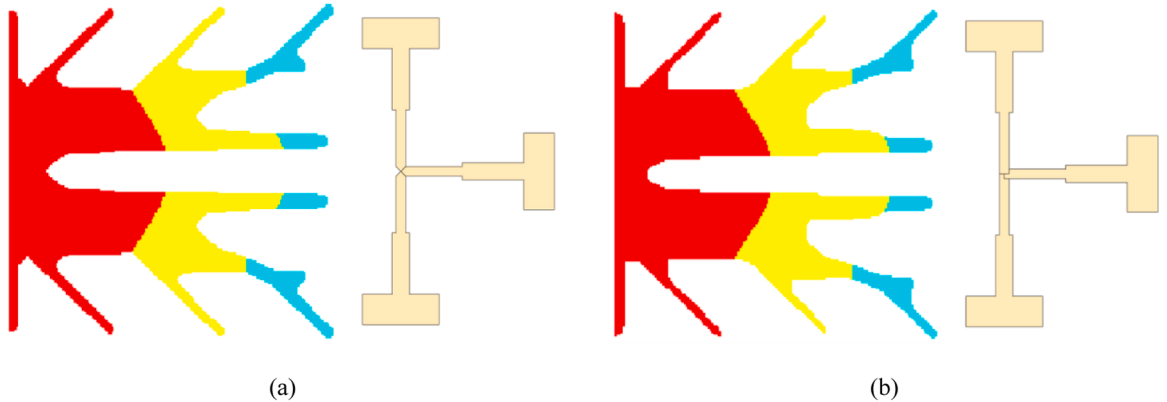


**Fig. 32.** The optimized designs obtained from HASM-OPT with the conic SM tool (a) and the flat SM tool (b).

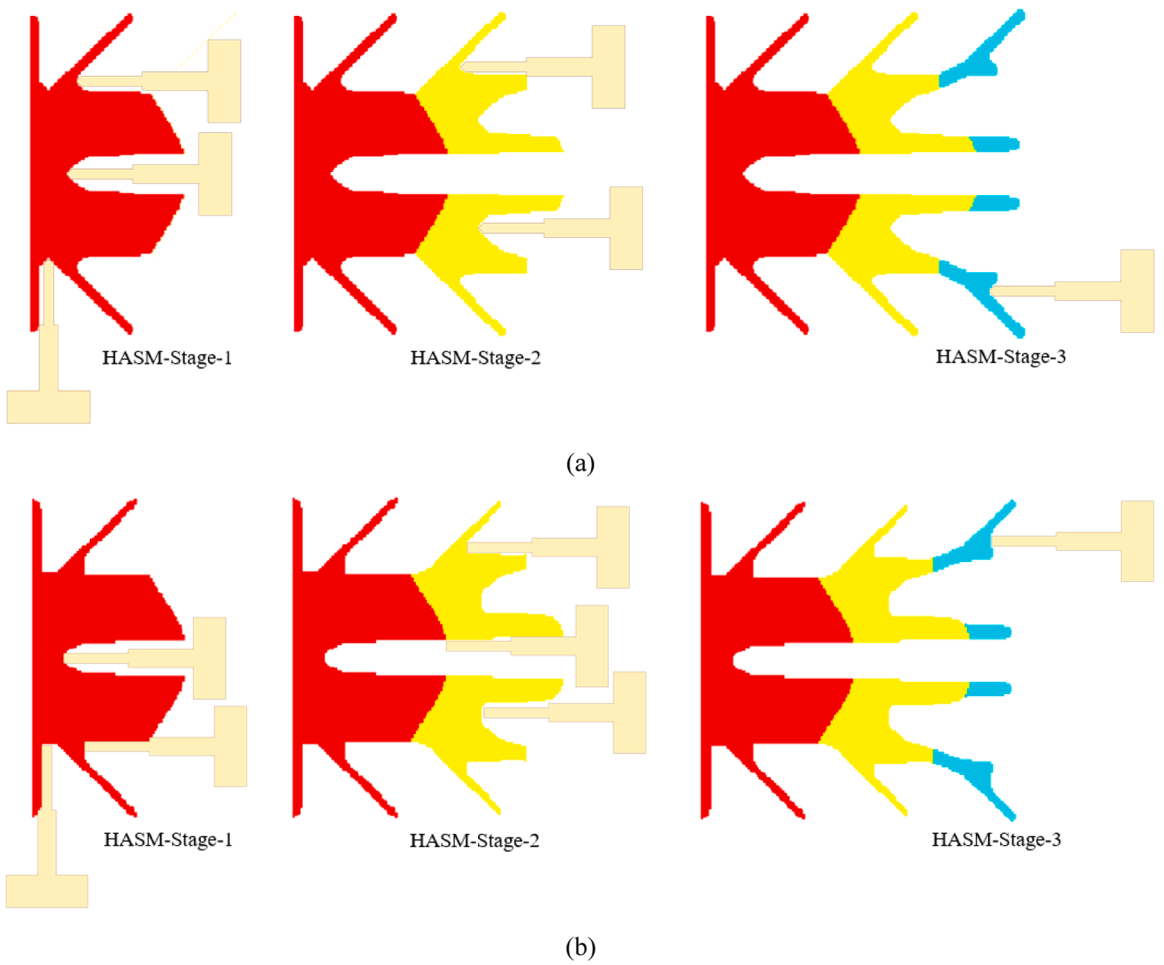


**Fig. 33.** The certain geometry at local areas due to the varying shape of the conic SM tool (a) and the flat SM tool (b).

of the optimized structures do not exhibit significant variations when alternative tools are employed. Moreover, the performances of these structures are quite similar, with thermal compliance values of 327.8891J, 321.3293J, and 318.440J.

However, certain differences emerge at local areas due to the varying shape of the tool tip, as depicted in Fig. 33. For instance, in the case of using the flat tool, it fails to produce the internal hole's sharp corner features that appear in other designs. This phenomenon arises from the fact that the flat-shaped tool tip cannot reach the sharp corners at the bottoms of the deep holes.

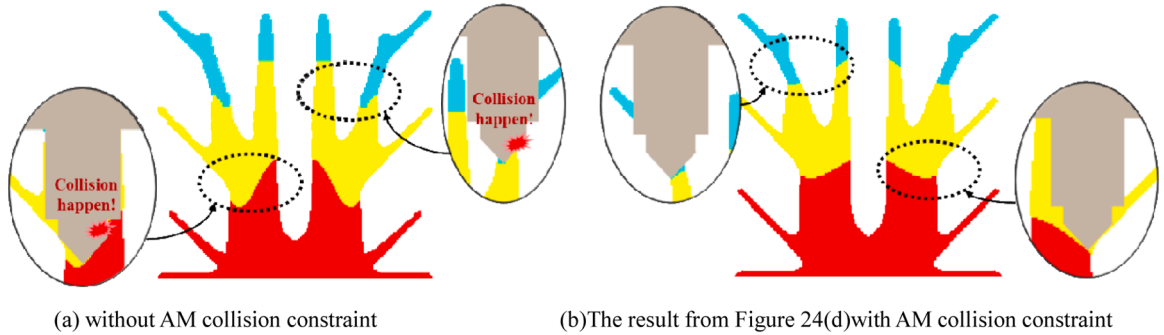


**Fig. 34.** The optimized design obtained from ProHASM-OPT for 3 stages without/with AM collision constraint.

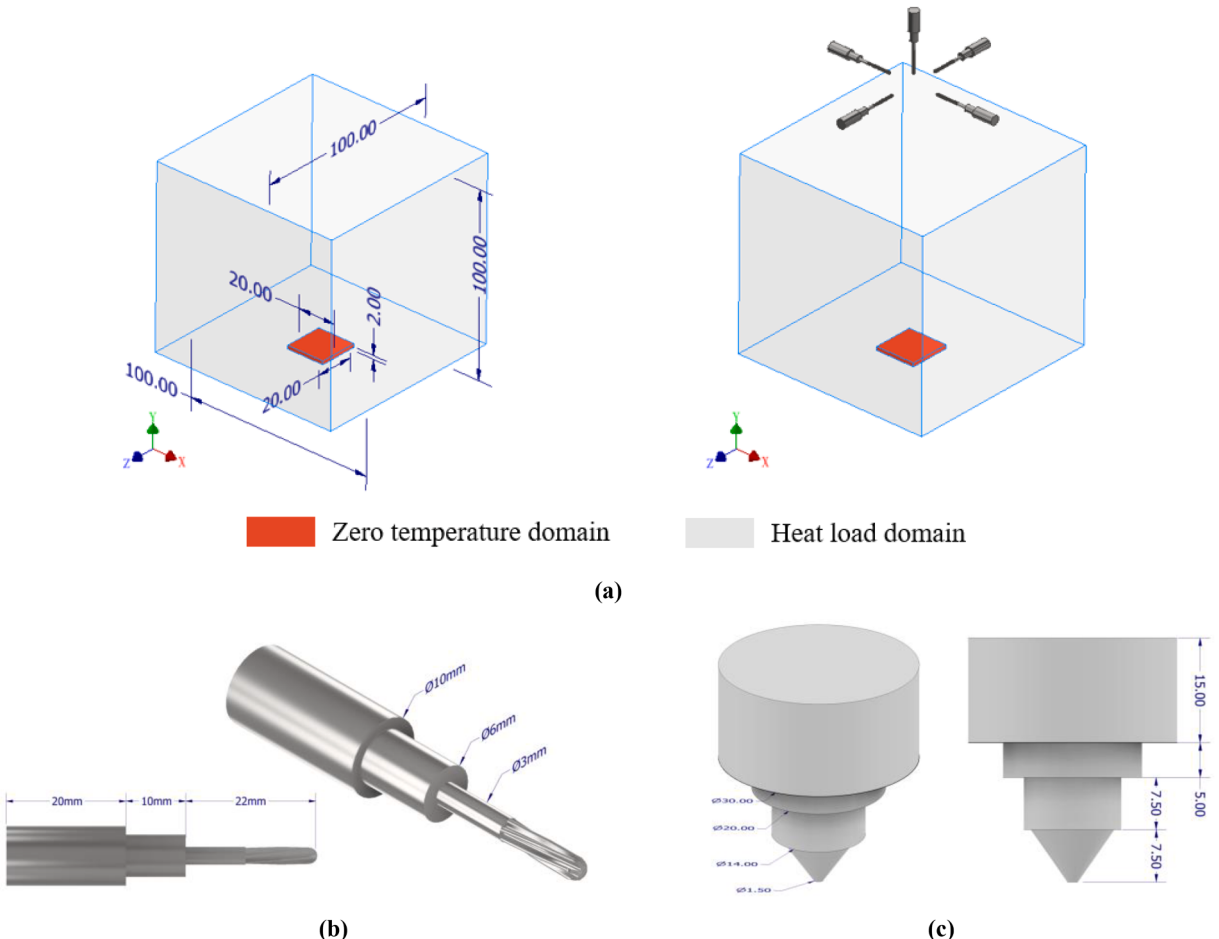


**Fig. 35.** The boundary condition and tool direction information for the 3D heat conduction example (a); and the geometries of the SM tool (b) and AM tool (c) in this case.

#### 5.1.5. The effect of AM tool collision constraint

In this Section, the effect of AM tool collision constraint is discussed. A new ProHASM-OPT case with three HASM stages and three SM tool orientations is provided here. In this case, the optimization model does not contain the AM tool collision constraint shown in Eq. (23), and its corresponding optimized design is illustrated in Fig. 34 (a).

As observed from Fig. 34, when the AM collision constraint is not involved, the material distributions for Fig. 34 (a) and (b) exhibit remarkable similarity. However, there are notable distinctions for the interface shape between the HASM subdivisions. In particular, abrupt transitions are observed between different HASM subdivisions in Fig. 34 (a). As the result, collisions are identified between the

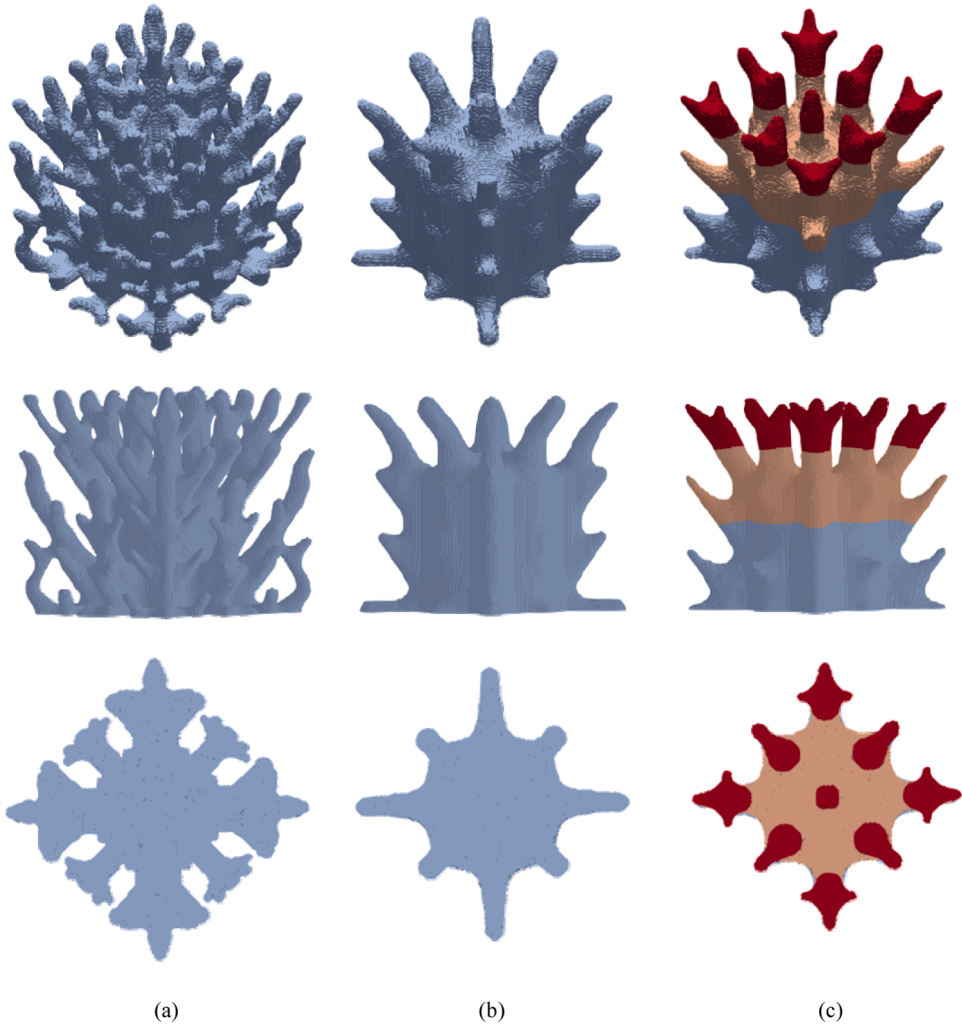


**Fig. 36.** The optimized design obtained from ProHASM-OPT with 3 stages and 5 SM tool directions.

AM tool and the pre-existing structure.

### 5.2. 3-D example

The 3D numerical example is also a heat conduction problem as shown in Fig. 35 (a), whose sizes are defined with  $L = 100\text{mm}$ ,  $W = 100\text{mm}$ ,  $H = 100\text{mm}$ . The build direction is bottom-up. A mesh with  $100 \times 100 \times 100$  cubic elements of size  $1\text{mm} \times 1\text{mm} \times 1\text{mm}$  is employed to discretize the design space. The mass fraction constraint for the structure is set to 25%.

In this example, the ProHASM-OPT optimization scheme with 3 HASM stages and 5 SM tool directions is under consideration. The shape information for both the SM tool and AM tool can be found in Fig. 35 (a) and (b). Fig. 37 (c) displays the geometric topology of the optimized structures, with the final thermal compliance of 116.742J. Meanwhile, the results obtained from AM-OPT and HASM-OPT are provided in Fig. 37 (a) and (b), and their final thermal compliance is 66.132J and 156.992J, respectively.

The temperature distribution maps from the three optimization schemes are displayed in Fig. 37. It can be seen that the structural performance of AM-OPT is the best, followed by ProHASM-OPT, while HASM-OPT performs the worst. This phenomenon is consistent with the results obtained in the previous 2D cases. Meanwhile, the cross-sectional views of the three results are displayed in Fig. 37. It can be observed that in the case of AM-OPT, the geometric complexity is the highest among the three schemes. However, as a consequence, many geometric features cannot be processed due to the inaccessibility of the cutting tool. Compared to HASM-OPT, ProHASM-OPT generates more intricate geometric features. Furthermore, in the top region of the structure, ProHASM-OPT can generate deeper geometric features. While for HASM-OPT case, such kind of geometry cannot appear due to the constraints imposed by the cutting tool's depth and shape.

Finally, historical data on the convergence of ProHASM-OPT is presented in Fig. 38. The optimization process terminates after 250 iterations. At this point, the objective function value has reached a stable state, and the multi-stage SM accessibility constraint, AM

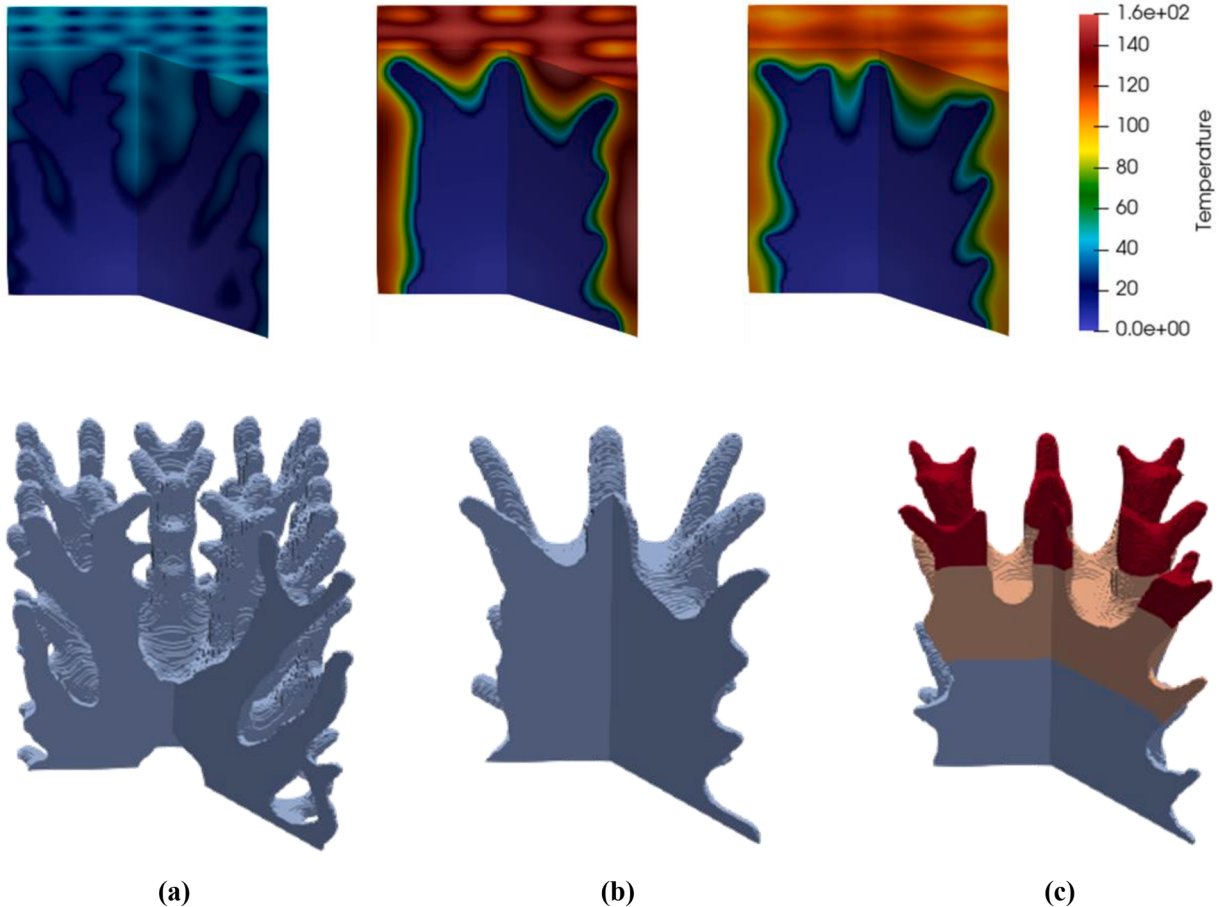


**Fig. 37.** The temperature distribution maps (top row), and the cross-sectional views maps (bottom row) for the designs in Fig. 37 (a)–(c).

collision constraint, and volume fraction constraint has all been substantially satisfied.

## 6. Experiment validation

HASM technique is mainly developed for metal parts. However, the DED-type metal 3D printing is coupled with complicated thermal-fluid-mechanical issues, causing cracks, over-distortion, insufficient height, interface bulge, etc. Hence, performing manufacturability validation based on metal HASM is associated with tedious process fine-tuning and high cost. Since the geometric accessibility and self-support issue is focused, we modify a small-sized 5-axis subtractive machine tool [31] by adding a switchable material extrusion module to 3D print plastic materials of PLA. Hence, the geometric validation can be conducted in a low cost manner while the effectiveness would not be compromised. The reinstalled machine tool and the additive-subtractive manufacturing process are demonstrated in Fig. 39.

To achieve the high surface precision by SM finishing, the structures produced by additive manufacturing are intentionally thickened than the designed structures (i.e., the dilated version  $\rho_d$ ). The difference between  $\rho_d$  and  $\rho$  indicates the materials that need to be removed through SM at each process stage. The results obtained from ProHASM-OPT optimization with 3 HASM stages and 5 SM tool directions (Fig. 36 (c)) is fabricated by the machine. The produced prototype is depicted in Fig. 40 (a) for which the part is successfully manufactured without encountering cutting tool interference. The results prove that the structure designed from our method is geometrically compatible to hybrid manufacturing. In comparison with Fig. 40 (b), a pure AM result, the hybrid manufactured part surface eliminates the stair case textures and also removes the local material accumulations due to deposition path turnings. Hence, the surface quality improvement is visibly identified. It is also noted that the prototype surface does not exhibit a completely smooth finish that, interfacial gaps can be seen due to transitioning the build directions. This is an issue related to multi-axis material extrusion that would not appear in laser-based metal AM.

The overall machining process is illustrated in Fig. 41, including three HASM stages. The majority of the solid part is processed at the first two stages, with 32.7 % completed after the first stage and 81.5 % after the second stage. In order to maximize the usable workspace and prevent collisions, the cutting tools for subtractive operations during the additive phase will be manually removed. Given that the tools have fixed positions of installation, the time required for their removal and reinstallation is minimal, and there is

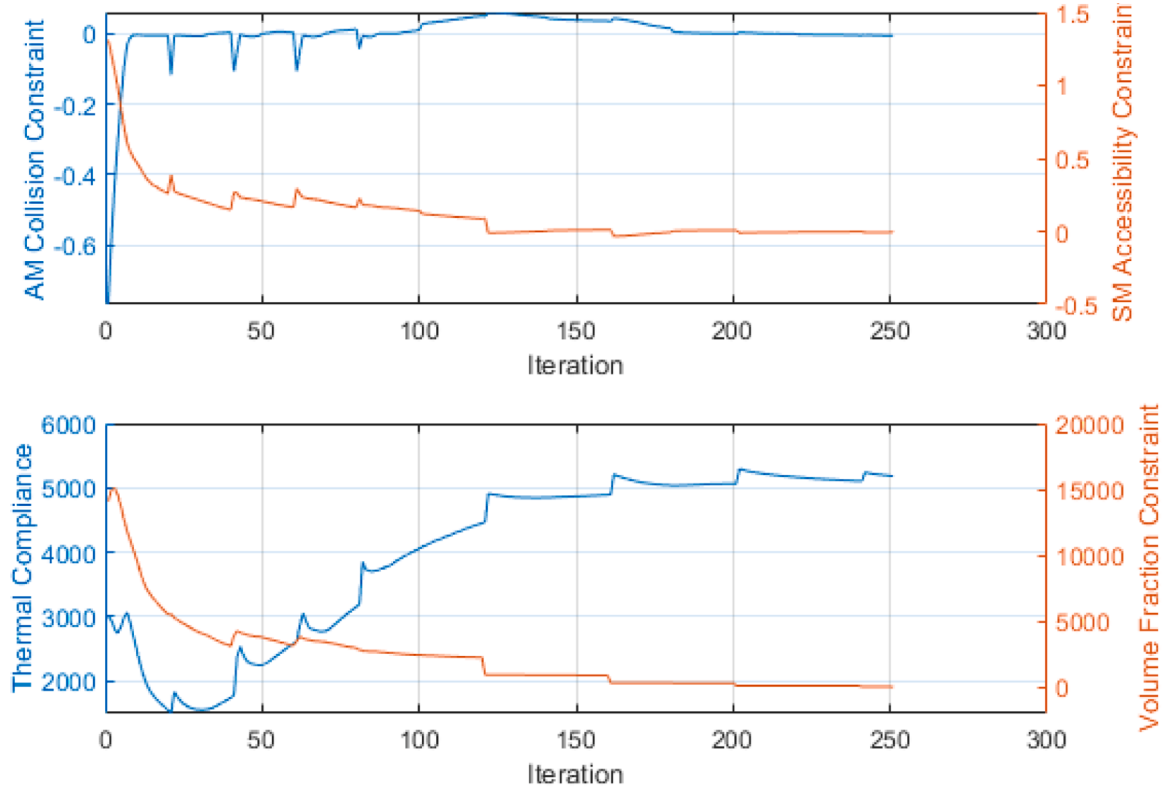


**Fig. 38.** The historical data of convergence information for the 3D ProHASM-OPT case.



**Fig. 39.** The reinstalled machine tool and the additive-subtractive manufacturing process.

no need for additional positioning calibration.

The CNC system utilized only allows for open/close operations to control the extruder. Consequently, we cannot perform retraction by reversing the extruder, leading to noticeable stringing during idle travel and subpar surface quality in the additive process. It is worth noting that this issue does not impact the final machining result, as any defects can be readily addressed during the subsequent subtractive steps. This, to some extent, emphasizes the value of HASM.

## 7. Conclusion

In this work, we have introduced a novel design approach for HASM-oriented topology optimization. This method effectively enables the synergistic optimization of structure and fabrication process plan, ensuring that the designed results can be successfully manufactured by HASM machines. Based on numerous numerical trials, we can draw the following conclusions:

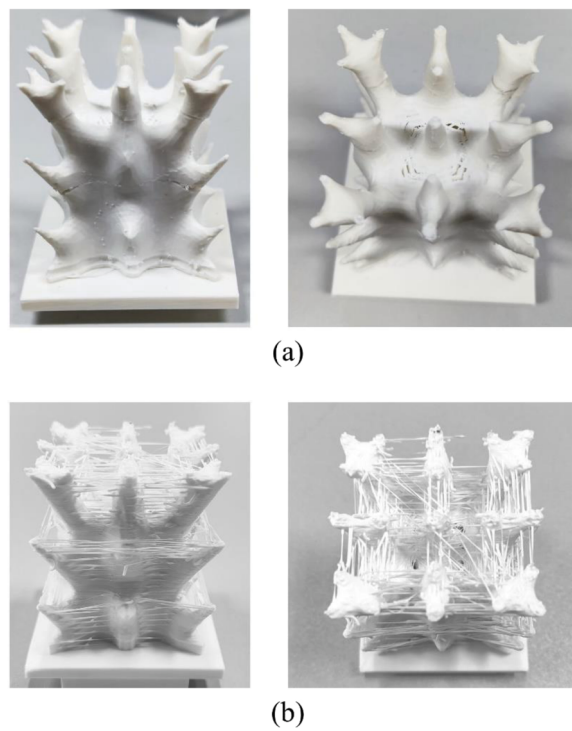


**Fig. 40.** The manufacturing quality comparison between the HASM result (a) and the pure AM result (b).

1. The proposed series of HASM-oriented geometric constraints can robustly prevent the designed structure and fabrication process plan from encountering issues related to subtractive tool inaccessibility and additive nozzle collision. These constraints also involve factors such as tool geometry and cutting depth that make them practically flexible.
2. New HASM-oriented geometric constraints introduced in this work are incorporated into the optimization process in the form of explicit volume constraints (subtractive accessibility constraint & additive collision-free constraint). As a result, this method can easily be extended to address other physical optimization objectives.
3. Compared to pure AM, parts produced using HASM exhibit higher dimensional accuracy and surface quality.
4. In contrast to designs aimed at single-step HASM processing, the designs obtained through the proposed method exhibit improved structural performance.

These findings highlight the effectiveness and advantages of our proposed approach for HASM-oriented design optimization. However, we must acknowledge that this work still has limitations, including:

1. Limited to 3-axis AM: The proposed method does not account for multi-axis AM. It defaults to the traditional bottom-up stacking approach, which, to a certain extent, restricts the degrees of design freedom.
2. Geometric constraints only: The method primarily considers geometric constraints, and it does not take into account the thermal-fluid-mechanical phenomena that may occur during the AM process, such as residual deformations and interfacial bulges.
3. Fixed number of HASM stages: In this method, the number of HASM stages cannot be optimized and must be predetermined.
4. All presented results are likely to be local optima, given the nonlinear, non-convex and large-scale nature of the involved optimization problems.

#### CRediT authorship contribution statement

**Shuzhi Xu:** Writing – original draft, Visualization, Validation, Software, Methodology, Investigation, Formal analysis, Data curation. **Jikai Liu:** Writing – review & editing, Supervision, Resources, Project administration, Methodology, Investigation, Funding acquisition, Conceptualization. **Kentaro Yaji:** Writing – review & editing, Supervision. **Lin Lu:** Visualization, Validation, Resources.

#### Declaration of competing interest

The authors declare that they have no known competing financial interests or personal relationships that could have appeared to influence the work reported in this paper.

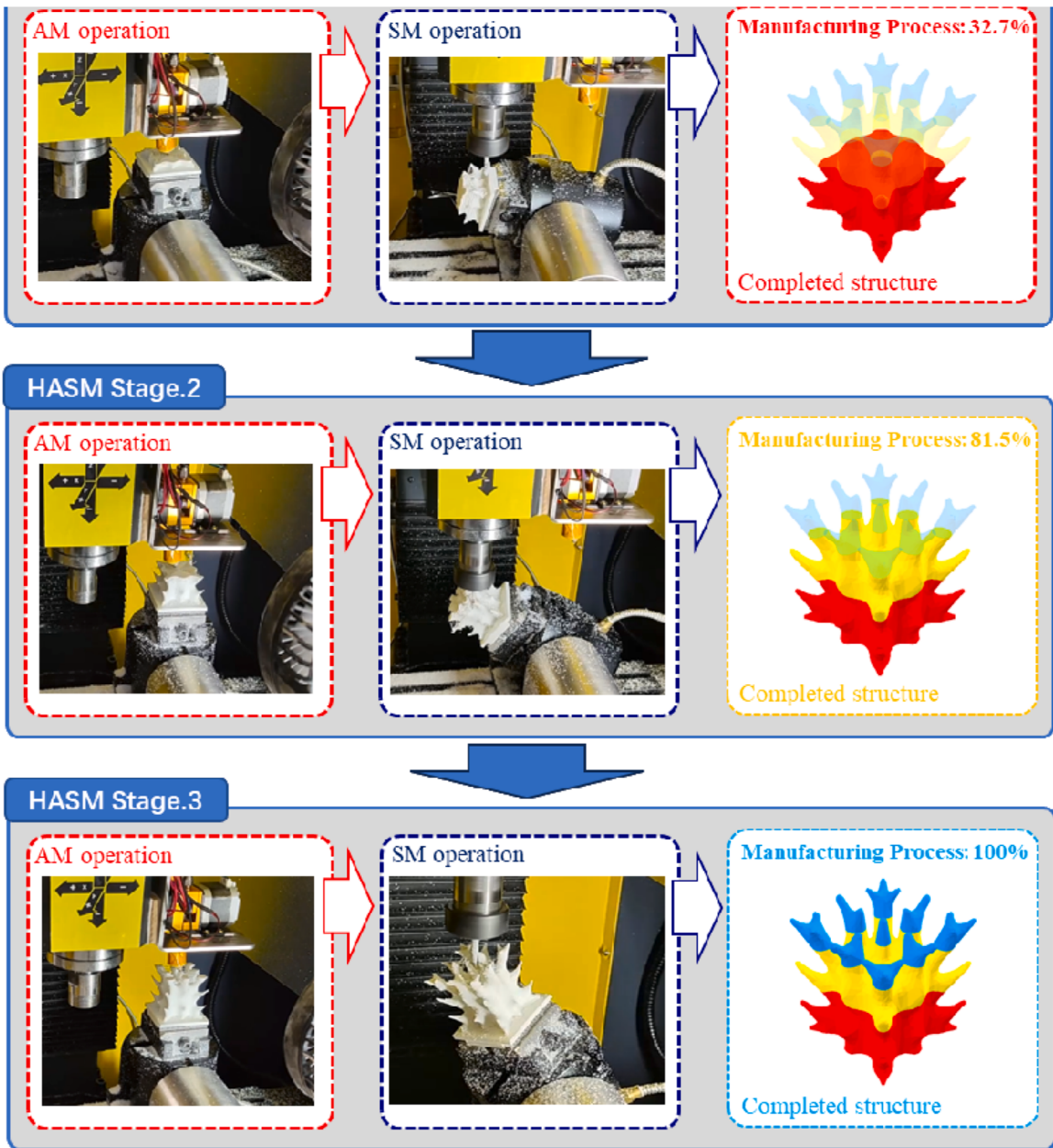


Fig. 41. The HASM manufacturing process for the result in Fig. 36(c).

#### Data availability

Data will be made available on request.

#### Acknowledgments

The authors would like to acknowledge the support from National Natural Science Foundation of China under Grant 52105462, and the support from Key R&D Program of Shandong Province, China (2021CXGC010206).

#### References

- [1] W. Grzesik, Hybrid additive and subtractive manufacturing processes and systems: a review, *J. Mach. Eng.* 18 (4) (2018) 5–24.

- [2] M. Merklein, D. Junker, A. Schaub, F. Neubauer, Hybrid additive manufacturing technologies—an analysis regarding potentials and applications, *Phys. Procedia* 83 (2016) 549–559.
- [3] U.M. Dilberooglu, B. Gharehpapagh, U. Yaman, M. Dolen, Current trends and research opportunities in hybrid additive manufacturing, *Int. J. Adv. Manuf. Technol.* 113 (2021) 623–648.
- [4] L. Li, A. Haghghi, Y. Yang, Theoretical modelling and prediction of surface roughness for hybrid additive–subtractive manufacturing processes, *IIE Trans. Part C: Prod. Eng.* 51 (2) (2019) 124–135.
- [5] S. Zhang, Y. Zhang, M. Gao, F. Wang, Q. Li, X. Zeng, Effects of milling thickness on wire deposition accuracy of hybrid additive/subtractive manufacturing, *Sci. Technol. Weld. Join.* 24 (5) (2019) 375–381.
- [6] P. Kunwar, Z. Xiong, S.T. McLoughlin, P. Soman, Oxygen-permeable films for continuous additive, subtractive, and hybrid additive/subtractive manufacturing, *3D Print. Addit. Manuf.* 7 (5) (2020) 216–221.
- [7] J. Liu, Y. Ma, A survey of manufacturing oriented topology optimization methods, *Adv. Eng. Softw.* 100 (2016) 161–175.
- [8] M. Zhou, R. Fleury, Y.K. Shyy, H. Thomas, J. Brennan, Progress in topology optimization with manufacturing constraints, in: Proceedings of the 9th AIAA/ISSMO Symposium on Multidisciplinary Analysis and Optimization, 2002, p. 5614.
- [9] L. Meng, W. Zhang, D. Quan, G. Shi, L. Tang, Y. Hou, P. Breitkopf, J. Zhu, T. Gao, From topology optimization design to additive manufacturing: Today's success and tomorrow's roadmap, *Arch. Comput. Methods Eng.* 27 (2020) 805–830.
- [10] T. Zegard, G.H. Paulino, Bridging topology optimization and additive manufacturing, *Struct. Multidiscip. Optim.* 53 (2016) 175–192.
- [11] D. Brackett, I. Ashcroft, R. Hague, Topology optimization for additive manufacturing, in: Proceedings of the 2011 International Solid Freeform Fabrication symposium, University of Texas at Austin, 2011.
- [12] Z.H.U. Jihong, Z.H.O.U. Han, W.A.N.G. Chuang, Z.H.O.U. Lu, Y.U.A.N. Shangqin, W. Zhang, A review of topology optimization for additive manufacturing: status and challenges, *Chin. J. Aeronaut.* 34 (1) (2021) 91–110.
- [13] J. Liu, A.T. Gaynor, S. Chen, Z. Kang, K. Suresh, A. Takezawa, L. Lei, J. Kato, J. Tang, C.C.L. Wang, L. Cheng, X. Liang, A. To, Current and future trends in topology optimization for additive manufacturing, *Struct. Multidiscip. Optim.* 57 (6) (2018) 2457–2483.
- [14] M.P. Bendsoe, O. Sigmund, *Topology Optimization: Theory, Methods, and Applications*, Springer Science & Business Media, 2003.
- [15] M.Y. Wang, X. Wang, D. Guo, A level set method for structural topology optimization, *Comput. Methods Appl. Mech. Eng.* 192 (1-2) (2003) 227–246.
- [16] T. Yamada, K. Izui, S. Nishiaki, A. Takezawa, A topology optimization method based on the level set method incorporating a fictitious interface energy, *Comput. Methods Appl. Mech. Eng.* 199 (45-48) (2010) 2876–2891.
- [17] X. Huang, Y.M. Xie, Bi-directional evolutionary topology optimization of continuum structures with one or multiple materials, *Comput. Mech.* 43 (2009) 393–401.
- [18] W. Zhang, J. Yuan, J. Zhang, X. Guo, A new topology optimization approach based on Moving Morphable Components (MMC) and the ersatz material model, *Struct. Multidiscip. Optim.* 53 (2016) 1243–1260.
- [19] Y.F. Fu, K. Long, B. Rolfe, On non-penalization SEMDOT using discrete variable sensitivities, *J. Optim. Theory Appl.* 198 (2) (2023) 644–677.
- [20] J. Liu, J. Huang, Y. Zheng, S. Hou, S. Xu, Y. Ma, C. Huang, B. Zou, L. Li, Challenges in topology optimization for hybrid additive-subtractive manufacturing: a review, *Comput. Aided Des.* (2023) 161–103531.
- [21] J.C. Heigel, T.Q. Phan, J.C. Fox, T.H. Gnaupe-Herold, Experimental investigation of residual stress and its impact on machining in hybrid additive/subtractive manufacturing, *Procedia Manuf.* 26 (2018) 929–940.
- [22] K.A. Lorenz, J.B. Jones, D.I. Wimpenny, M.R. Jackson, A review of hybrid manufacturing, in: Proceedings of the 2014 International Solid Freeform Fabrication Symposium, University of Texas at Austin, 2015.
- [23] G. Manogharan, R.A. Wyk, O.L. Harrysson, Additive manufacturing–integrated hybrid manufacturing and subtractive processes: economic model and analysis, *Int. J. Comput. Integr. Manuf.* 29 (5) (2016) 473–488.
- [24] L. Chen, K. Xu, K. Tang, Optimized sequence planning for multi-axis hybrid machining of complex geometries, *Comput. Graph.* 70 (2018) 176–187.
- [25] W. Zhang, M. Soshi, K. Yamazaki, Development of an additive and subtractive hybrid manufacturing process planning strategy of planar surface for productivity and geometric accuracy, *Int. J. Adv. Manuf. Technol.* 109 (2020) 1479–1491.
- [26] N. Chen, M. Frank, Process planning for hybrid additive and subtractive manufacturing to integrate machining and directed energy deposition, *Procedia Manuf.* 34 (2019) 205–213.
- [27] X. Xiao, S. Joshi, Decomposition and sequencing for a 5-axis hybrid manufacturing process, in: Proceedings of the International Manufacturing Science and Engineering Conference 84256, American Society of Mechanical Engineers, 2020, p. 49.
- [28] L. Chen, T.Y. Lau, K. Tang, Manufacturability analysis and process planning for additive and subtractive hybrid manufacturing of Quasi-rotational parts with columnar features, *Comput. Aided Des.* 118 (2020) 102759.
- [29] G.P. Harabin, M. Behandish, Hybrid manufacturing process planning for arbitrary part and tool shapes, *Comput. Aided Des.* 151 (2022) 103299.
- [30] M. Behandish, S. Nelaturi, J. de Kleer, Automated process planning for hybrid manufacturing, *Comput. Aided Des.* 102 (2018) 115–127.
- [31] F. Zhong, H. Zhao, H. Li, X. Yan, J. Liu, B. Chen, L. Lu, VASCO: volume and surface co-decomposition for hybrid manufacturing, *ACM Trans. Graph. TOG* 42 (6) (2023) 1–17.
- [32] J. Liu, J. Huang, J. Yan, L. Li, S. Li, Full sensitivity-driven gap/overlap free design of carbon fiber-reinforced composites for 3D printing, *Appl. Math. Model.* 103 (2022) 308–326.
- [33] J. Liu, A.C. To, Deposition path planning-integrated structural topology optimization for 3D additive manufacturing subject to self-support constraint, *Comput. Aided Des.* 91 (2017) 27–45.
- [34] Y. Guo, R. Ahmad, Y. Ma, Topology optimization of the vibrating structure for fused deposition modelling of parts considering a hybrid deposition path pattern, *Int. J. Comput. Integr. Manuf.* 36 (9) (2023) 1379–1396.
- [35] S. Xu, J. Huang, J. Liu, Y. Ma, Topology optimization for FDM parts considering the hybrid deposition path pattern, *Micromachines* 11 (8) (2020) 709 (Basel).
- [36] J. Robinson, I. Ashton, P. Fox, E. Jones, C. Sutcliffe, Determination of the effect of scan strategy on residual stress in laser powder bed fusion additive manufacturing, *Addit. Manuf.* 23 (2018) 13–24.
- [37] W. Zhang, M. Tong, N.M. Harrison, Scanning strategies effect on temperature, residual stress and deformation by multi-laser beam powder bed fusion manufacturing, *Addit. Manuf.* 36 (2020) 101507.
- [38] X. Liang, W. Dong, Q. Chen, A.C. To, On incorporating scanning strategy effects into the modified inherent strain modeling framework for laser powder bed fusion, *Addit. Manuf.* 37 (2021) 101648.
- [39] Q. Chen, H. Taylor, A. Takezawa, X. Liang, X. Jimenez, R. Wicker, A.C. To, Island scanning pattern optimization for residual deformation mitigation in laser powder bed fusion via sequential inherent strain method and sensitivity analysis, *Addit. Manuf.* 46 (2021) 102116.
- [40] S. Xu, J. Huang, J. Liu, Y. Ma, J. Liu, An island scanning path-pattern optimization for metal additive manufacturing based on inherent strain method, *Comput. Aided Des. Appl.* 19 (2022) 812–824.
- [41] O. Ibhade, Z. Zhang, J. Sixt, K.M. Nsiempba, J. Orakwe, A. Martinez-Marchese, O. Ero, S. Shahabad, A. Bonakdar, E. Toyserkani, Topology optimization for metal additive manufacturing: current trends, challenges, and future outlook, *Virtual Phys. Prototyp.* 18 (1) (2023) e2181192.
- [42] A. Takezawa, A.C. To, Q. Chen, X. Liang, F. Dugast, X. Zhang, M. Kitamura, Sensitivity analysis and lattice density optimization for sequential inherent strain method used in additive manufacturing process, *Comput. Methods Appl. Mech. Eng.* 370 (2020) 113231.
- [43] S. Xu, J. Liu, Y. Ma, Residual stress constrained self-support topology optimization for metal additive manufacturing, *Comput. Methods Appl. Mech. Eng.* 389 (2022) 114380.
- [44] T. Miki, T. Yamada, Topology optimization considering the distortion in additive manufacturing, *Finite Elem. Anal. Des.* 193 (2021) 103558.
- [45] G. Misun, E. van de Ven, M. Langelaar, H. Geijsselaers, F. van Keulen, T. van den Boogaard, C. Ayas, Topology optimization for additive manufacturing with distortion constraints, *Comput. Methods Appl. Mech. Eng.* 386 (2021) 114095.

- [46] A. Takezawa, H. Guo, R. Kobayashi, Q. Chen, A.C. To, Simultaneous optimization of hatching orientations and lattice density distribution for residual warpage reduction in laser powder bed fusion considering layerwise residual stress stacking, *Addit. Manuf.* 60 (2022) 103194.
- [47] S. Xu, J. Liu, X. Li, Y. Ma, Concurrent Island scanning pattern and large-scale topology optimization method for laser powder bed fusion processed parts, *Finite Elem. Anal. Des.* 225 (2023) 104018.
- [48] Y. Liu, X. Huang, Y. Xiong, M. Zhou, Z. Lin, Concurrent topology optimization of parts and their supports for additive manufacturing with thermal deformation constraint, *Comput. Struct.* 289 (2023) 107146.
- [49] J. Liu, Y.S. Ma, 3D level-set topology optimization: a machining feature-based approach, *Struct. Multidiscip. Optim.* 52 (2015) 563–582.
- [50] W.D. Li, S.K. Ong, A.Y. Nee, Recognizing manufacturing features from a design-by-feature model, *Comput. Aided Des.* 34 (11) (2002) 849–868.
- [51] H. Deng, P.S. Vulimiri, A.C. To, CAD-integrated topology optimization method with dynamic extrusion feature evolution for multi-axis machining, *Comput. Methods Appl. Mech. Eng.* 390 (2022) 114456.
- [52] J. Liu, H. Yu, Y. Ma, Minimum void length scale control in level set topology optimization subject to machining radii, *Comput. Aided Des.* 81 (2016) 70–80.
- [53] M. Langelaar, Topology optimization for multi-axis machining, *Comput. Methods Appl. Mech. Eng.* 351 (2019) 226–252.
- [54] A.M. Mirzendehdel, M. Behandish, S. Nelaturi, Topology optimization with accessibility constraint for multi-axis machining, *Comput. Aided Des.* 122 (2020) 102825.
- [55] H. Deng, A.C. To, A novel mathematical formulation for density-based topology optimization method considering multi-axis machining constraint, *J. Mech. Des.* 144 (6) (2022) 061702.
- [56] H.Y. Lee, M. Zhu, J.K. Guest, Topology optimization considering multi-axis machining constraints using projection methods, *Comput. Methods Appl. Mech. Eng.* 390 (2022) 114464.
- [57] J. Gasick, X. Qian, Simultaneous topology and machine orientation optimization for multiaxis machining, *Int. J. Numer. Methods Eng.* 122 (24) (2021) 7504–7535.
- [58] J. Liu, C. Zhang, B. Zou, L. Li, H. Yu, Topology optimization for vat photopolymerization 3D printing of ceramics with flushing jet accessibility constraint, *Virtual Phys. Prototyp.* 19 (1) (2024) e2303717.
- [59] G. Allaire, M. Bihl, B. Bogosel, M. Godey, Accessibility constraints in structural optimization via distance functions, *J. Comput. Phys.* 484 (2023) 112083.
- [60] N. Morris, A. Butscher, F. Iorio, A subtractive manufacturing constraint for level set topology optimization, *Struct. Multidiscip. Optim.* 61 (4) (2020) 1573–1588.
- [61] J. Liu, A.C. To, Topology optimization for hybrid additive-subtractive manufacturing, *Struct. Multidiscip. Optim.* 55 (2017) 1281–1299.
- [62] Y.S. Han, B. Xu, L. Zhao, Y.M. Xie, Topology optimization of continuum structures under hybrid additive-subtractive manufacturing constraints, *Struct. Multidiscip. Optim.* 60 (2019) 2571–2595.
- [63] J. Liu, Y. Zheng, Y. Ma, A. Qureshi, R. Ahmad, A topology optimization method for hybrid subtractive-additive remanufacturing, *Int. J. Precis. Eng. Manuf. Green Technol.* 7 (2020) 939–953.
- [64] A.M. Mirzendehdel, M. Behandish, S. Nelaturi, Topology optimization for manufacturing with accessible support structures, *Comput. Aided Des.* 142 (2022) 103117.
- [65] A.M. Mirzendehdel, M. Behandish, S. Nelaturi, Optimizing build orientation for support removal using multi-axis machining, *Comput. Graph.* 99 (2021) 247–258.
- [66] A.R. Gersborg, C.S. Andreasen, An explicit parameterization for casting constraints in gradient driven topology optimization, *Struct. Multidiscip. Optim.* 44 (2011) 875–881.
- [67] B.S. Lazarov, O. Sigmund, Filters in topology optimization based on Helmholtz-type differential equations, *Int. J. Numer. Methods Eng.* 86 (6) (2011) 765–781.
- [68] F. Wang, B.S. Lazarov, O. Sigmund, On projection methods, convergence and robust formulations in topology optimization, *Struct. Multidiscip. Optim.* 43 (2011) 767–784.
- [69] W. Wang, D. Munro, C.C. Wang, F. van Keulen, J. Wu, Space-time topology optimization for additive manufacturing: Concurrent optimization of structural layout and fabrication sequence, *Struct. Multidiscip. Optim.* 61 (2020) 1–18.
- [70] J.K. Guest, J.H. Prévost, T. Belytschko, Achieving minimum length scale in topology optimization using nodal design variables and projection functions, *Int. J. Numer. Methods Eng.* 61 (2) (2004) 238–254.
- [71] M. Langelaar, Topology optimization of 3D self-supporting structures for additive manufacturing, *Addit. Manuf.* 12 (2016) 60–70.
- [72] M. Langelaar, An additive manufacturing filter for topology optimization of print-ready designs, *Struct. Multidiscip. Optim.* 55 (2017) 871–883.